The Astrophysical Journal, 646:754–773, 2006 August 1

THE STAR-FORMING TORUS AND STELLAR DYNAMICAL BLACK HOLE MASS IN THE SEYFERT 1 NUCLEUS OF NGC 3227[1]

R. I. Davies,[2] J. Thomas,[2,3] R. Genzel,[2,4] F. Mueller Sánchez,[2] L. J. Tacconi,[2] A. Sternberg,[5] F. Eisenhauer,[2] R. Abuter,[2] R. Saglia,[2,3] and R. Bender[2,3]

Received 2005 September 26; accepted 2006 April 5

ABSTRACT

We report $R \sim 4300$ VLT SINFONI adaptive optics integral field K-band spectroscopy of the nucleus of the Seyfert 1 galaxy NGC 3227 at a spatial resolution of 0.″085 (7 pc). We present the morphologies and kinematics of emission lines and absorption features and give the first derivation of a black hole mass in a Seyfert 1 nucleus from stellar dynamics (marginally resolving the black hole's sphere of influence). We show that the gas in the nucleus has a mean column density of order 10^{24} cm^{-2} and that it is geometrically thick, in agreement with the standard "molecular torus" scenario. We discuss possible heating processes responsible for maintaining the vertical height of the torus. We also resolve the nuclear stellar distribution and find that within a few parsecs of the AGN there has been an intense starburst, the most recent episode of which began ~40 Myr ago but has now ceased. The current luminosity of stars within 30 pc of the AGN, $\sim 3 \times 10^9\ L_\odot$, is comparable to that of the AGN. We argue that the star formation has been occurring in the obscuring material. Finally, we apply Schwarzschild orbit superposition models to our full two-dimensional data and derive the mass of the black hole, paying careful attention to the input parameters, which are often uncertain. Our models yield a 1 σ range for the black hole mass of $M_{\rm BH} = 7 \times 10^6$–$2 \times 10^7\ M_\odot$.

Subject headings: galaxies: active — galaxies: individual (NGC 3227) — galaxies: nuclei — galaxies: Seyfert — galaxies: starburst — infrared: galaxies

Online material: color figures

1. INTRODUCTION

Three issues concerning active galactic nuclei (AGNs) that are currently receiving considerable attention, and which we address in this paper, are as follows: the relationship of the AGN to the surrounding star formation, the central black hole mass, and the physical properties of the obscuring torus.

The issue of star formation in AGNs has long been contentious, although it is now clear that on 0.1–1 kpc scales star formation is an important process in all types of AGNs (Cid Fernandes 2004). In particular, empirical population synthesis of Seyfert 2 nuclei (Cid Fernandes et al. 2001; González Delgado et al. 2001; Storchi-Bergmann et al. 2001) reveals evidence for recent (<1 Gyr) star formation within a few hundred parsecs of the nuclei in about 40% of Seyfert 2 nuclei. While some authors (e.g., Johuet et al. 2001; Gu et al. 2001) reach similar conclusions, not all concur (Ivanov et al. 2000). Mid- and far-infrared *Infrared Space Observatory* (*ISO*) data (Verma et al. 2005) also have much to offer on this issue. The situation regarding Seyfert 1 nuclei is rather more uncertain, and a criticism (equally applicable to Seyfert 2 galaxies) often leveled is that it lies so far from the AGN that it cannot be associated with or strongly influencing the characteristics of the AGN (Heckman et al. 1997). Nevertheless, Davies et al. (2004a, 2004b) report two cases where powerful starbursts do exist within the central few tens of parsecs of type 1 AGNs.

Beyond this debate is the fundamental question concerning the physics linking the two phenomena through a causal relationship (Shlosman & Begelman 1989; Goodman & Tan 2004; Thompson et al. 2005), which is related to, although more complex than, driving gas to small scales. While observation and theory provide strong indications linking gas inflow and circumnuclear starbursts to AGNs and nuclear starbursts, the statistical evidence is tenuous (Knapen 2004; Wada 2004; Shlosman 2003). For example, *Hubble Space Telescope* (*HST*) imaging shows no dependence of AGN activity on the presence of a nuclear spiral (Martini et al. 2003). Similarly, AGNs are equally common in galaxies with and without a compact nuclear gas component (García-Burillo et al. 2003).

A parallel theme is the molecular obscuring torus (Antonucci & Miller 1985; Antonucci 1993), the heart of the unification scheme. Many models of the thermally reradiated spectrum of the putative torus have been constructed, both as a uniform ring (Pier & Krolik 1992b, 1993; Granato & Danese 1994; Schartmann et al. 2005) and also as a clumpy medium (Nenkova et al. 2002), as was proposed for NGC 1068 a decade earlier by Cameron et al. (1993). In all cases, the crucial properties are a spatial scale of tens (to perhaps hundreds) of parsecs, a vertically extended geometry, and a high column density. In the last few years, models have begun to consider star formation within the torus (Wada & Norman 2002; Thompson et al. 2005), giving credence, albeit with a different perspective, to some early ideas about stellar light in AGN spectra.

The mass of the central supermassive black hole $M_{\rm BH}$ is the third issue we address. The masses of black holes in nearby AGNs are most commonly estimated by reverberation mapping (Onken et al. 2004), a technique that can be extended to higher redshift via additional scaling relations (Kaspi et al. 2000, 2005; Vestergaard 2002, 2004). Providing an independent measure of $M_{\rm BH}$ for reverberation masses would allow one to begin to understand the

[1] Based on observations at the European Southern Observatory VLT (074.B-9012).

[2] Max-Planck-Institut für extraterrestrische Physik, Postfach 1312, 85741 Garching, Germany.

[3] Universitäts-Sternwarte, Scheinerstrasse 1, 81679 Munich, Germany.

[4] Department of Physics, University of California, 366 Le Conte Hall, Berkeley, CA 94720-7300.

[5] School of Physics and Astronomy, Tel Aviv University, Tel Aviv 69978, Israel.

geometry of the broad-line region, which is the limiting factor in the accuracy of the method (Horne et al. 2004).

Estimates of such masses are important with respect to the relation between the $M_{\rm BH}$ in the center of a stellar spheroid and the velocity dispersion σ_* (Ferrarese & Merritt 2000; Gebhardt et al. 2000). This relation has superseded similar ones using the luminosity or mass of the spheroid (Kormendy & Richstone 1995; Magorrian et al. 1998) to become a cornerstone in the cosmological context of galaxy evolution and black hole growth. It is generally accepted that the $M_{\rm BH}$-σ_* relation should be valid for all spheroids irrespective of whether the black hole is quiescent or active, whether the spheroid in which it lies is a globular cluster or a giant elliptical galaxy, whether the spheroid is embedded in a gaseous disk or not, and so on. However, almost without exception the black hole masses that are considered "reliable" (typically those based on stellar kinematics and for which the radius of influence of the black hole has been resolved) have been derived only for nearby bulge-dominated E/S0 galaxies (Tremaine et al. 2002; Marconi & Hunt 2003; Ferrarese & Ford 2005). The smaller bulges of spiral galaxies imply lower $M_{\rm BH}$, making it difficult to spatially resolve the stellar kinematics. And for AGNs, where the black hole is by definition active rather than quiescent, the glare of the AGN itself is an added obstruction. To date there is only one such published mass, $\sim 2 \times 10^8\ M_\odot$ for Cen A (Silge et al. 2005). Despite this galaxy's proximity, seeing-limited observations are only able to resolve the radius of influence of the black hole because the black hole is at least 5 times more massive than expected from the $M_{\rm BH}$-σ_* relation. Given this result, it is crucial that black hole masses are derived using stellar kinematics at high spatial resolution for more AGNs.

In this paper we look in detail at these topics for the Seyfert 1 nucleus of NGC 3227. We probe the star formation and molecular gas in the central 80 pc at a spatial resolution of only a few parsecs. In particular, we discuss how the young stars and gas relate to our understanding of the canonical torus. In addition, we derive the mass of the black hole from Schwarzschild modeling of the stellar dynamics. This is the first time that this has been possible for a Seyfert 1 galaxy, where using integral field capability we measure the kinematics across the full two-dimensional field. We pay careful attention to issues that are often rather uncertain in Schwarzschild orbit superposition models: the inclination of the system, the mass-to-light ratio, and the contribution of gas to the gravitational potential.

The distance to NGC 3227 of 17 Mpc (for $H_0 = 70$–$75\ {\rm km\ s^{-1}\ Mpc^{-1}}$) is estimated from the 1250 km s^{-1} luminosity-weighted average velocity of the 13 galaxies in the group of which it is a member (Garcia 1993). Its infrared (8–1000 μm) luminosity is then $\log (L_{\rm IR}/L_\odot) = 9.93$. However, this does not represent the bolometric luminosity since the spectral energy distribution λF_λ is approximately flat in the range 0.3–1000 μm, and perhaps to even shorter wavelengths. Taking this into account, we estimate the bolometric luminosity to be $\log (L_{\rm bol}/L_\odot) = 10.2$.

2. OBSERVATIONS AND DATA REDUCTION

The data presented here were obtained on 2004 December 21 using SINFONI (Eisenhauer et al. 2003a; Bonnet et al. 2004) on the VLT UT4. The instrument consists of a cryogenic near-infrared integral field spectrometer SPIFFI (Eisenhauer et al. 2003a, 2003b) coupled to a visible curvature adaptive optics (AO) system (Bonnet et al. 2003). The AO module was able to correct on the nucleus of NGC 3227 (for which it measured $R = 13.9$ mag) in seeing of $\sim$0.″6, to reach nearly the diffraction limit of the telescope in the K band (an estimated 15% Strehl). With the appropriate pixel scale selected, the spectrograph was able, in a single shot, to obtain spectra covering the whole of the K band (approximately 1.95–2.45 μm) at a spectral resolution of $R \sim 4300$ for each 0.″0125 × 0.″025 pixel in a 0.″80 × 0.″80 field of view. A total of three sky and six on-source exposures of 600 s each, dithered by up to 0.″2, were combined to make the final data cube.

The data were reduced using the SINFONI custom reduction package SPRED. This performs all of the usual steps needed to reduce near-infrared spectra, but with additional routines for reconstructing the data cube. Because the sky airglow did not vary much during the observations and is low compared to the read noise at such small pixel scales, it was possible to make a combined sky frame that could be subtracted from all of the on-source frames without leaving OH line residuals. Following this step, the frames were flat-fielded and corrected for dead/hot pixels. The data were then interpolated to linear wavelength and spatial scales, after which the slitlets were aligned and stacked up to create a cube. Finally, the atmospheric absorption was compensated using the B9 star HD 83434, and flux calibration was performed using HD 83434 ($K = 6.917$) and HD 87015 ($K = 6.144$), which both yielded a zero point of 16.08 mag.

Spatial resolution.—No additional point-spread function (PSF) calibration frames using stars were taken. This is primarily because, although in principle one can match the brightness of a calibration star on the wave front sensor to the AGN, it is not possible to replicate either the spatial extent of the AGN or the background galaxy light associated with it. Together with changes in the ambient seeing that can occur on relatively fast timescales, this can result in a potentially considerable mismatch between the science and calibration PSFs (Davies et al. 2004c). Since, for the analysis presented here, a highly accurate PSF is not needed, we have instead made use of the broad Brγ emission, which is unresolved: it has been measured to be of order 0.02 pc by Salamanca et al. (1994) and Onken et al. (2003). This has the advantage of providing the resolution directly from the science frames and includes all effects associated with shifting and combining the cube, as well as smoothing (a 0.″0375 × 0.″0375 median filter was applied to the final cube). The PSF we use for convolving our models is then approximated by a symmetrical fit to the broad Brγ emission as shown in Figure 1. In this figure we have plotted the value for every pixel within 0.″3 of the center, from which it can be seen that there are no asymmetric artifacts resulting from the AO correction. Overdrawn are both Gaussian and Moffat profiles. The latter, as expected, matches the faint extended wings in the profile, but both reproduce the core of the profile equally well. They yield an FWHM resolution of 0.″085.

Derivation of the kinematics and their uncertainties.—The velocity and dispersion of the emission lines are found by simultaneously fitting the continuum level with a linear function and the line itself with a Gaussian. The uncertainty of the fit is estimated using Monte Carlo techniques assuming that the noise is uncorrelated and the line is well represented by a Gaussian. The method involves adding a Gaussian with the measured properties to a spectral segment with the same noise statistics as the data and refitting the line to yield a new set of Gaussian parameters. After repeating this 100 times, the standard deviation of the center and dispersion are used as the uncertainties for the velocity and line width.

The shape of the CO absorption band heads in a galaxy spectrum arises from the intrinsic spectral profile of the stars themselves convolved with a broadening profile that carries the information about the kinematics. The use of template stars (we

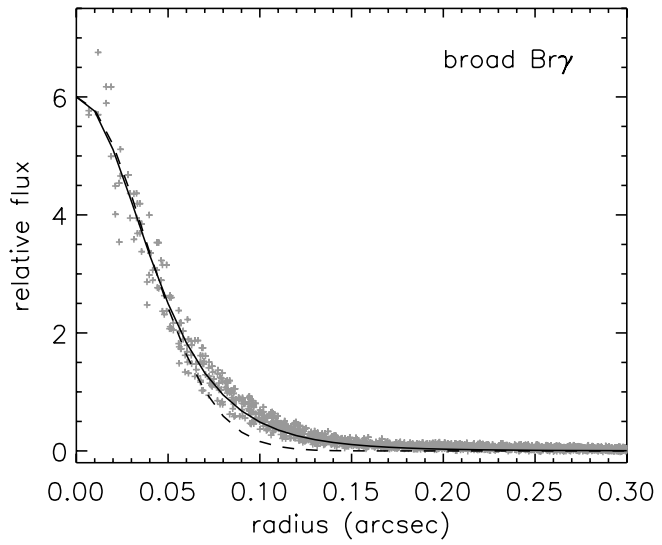

FIG. 1.—Azimuthally averaged profile of the broad Brγ line map, used to estimate the spatial resolution. The data points (values for every pixel within 0.″3 of the center) are marked as gray crosses and show no asymmetric artifacts that could result from the AO correction. Overdrawn is a Gaussian profile (*dashed line*) and a Moffat profile (*solid line*). Although the latter better reproduces the wings in the profile, both appear to be reasonable approximations to the profile and both yield the same FWHM resolution of 85 mas.

chose the K0 I star HD 179323) allows one to separate these two components. One technique commonly used is deconvolution with the Fourier cross-correlation quotient method. The principal advantage of this method is that it allows one to recover the full broadening profile even if it is not well represented by a function such as a Gaussian (plus Hermite terms). However, because the Fourier transform of the object is divided by that of the template, the noise is amplified, and while it can be reduced by Wiener filtering, setting the optimal parameters of the filter is only possible if the noise and signal can be properly distinguished in Fourier space. If this is not done correctly, it can be difficult to obtain the correct object dispersion. The alternative is to convolve the template with an analytical function and iteratively minimize its difference to the object using a χ^2 criterion. The limitation of this technique is its speed and the fact that the convolution function needs to be relatively simple. On the other hand, it is less adversely affected by noisy data and one can easily reject bad data values. In addition, it provides a clear path to estimating the uncertainties using standard techniques. One can estimate the confidence level for each parameter separately by finding the value for which, with all of the other parameters reoptimized, χ^2 increases by 1.

It is the latter method that we have used because the individual spectra for each spatial pixel are rather noisy, and we only extract the usual three parameters for a Gaussian fit. Tests have shown that for these data it is not possible to determine coefficients for the Hermite polynomials that would indicate the deviations from a Gaussian.

We have only made use of the first (i.e., CO 2–0) band head because [Ca VIII] emission at the edge of the CO 3–1 strongly biases the derived velocities (making them much more positive where the line emission is strongest) when this second band head is used. The third CO 4–2 band head adds very little because it is strongly affected by residual atmospheric features.

Smoothing.—All of the images presented in this paper have been smoothed using optimal Voronoi tessellations, as described and implemented by Cappellari & Copin (2003). This scheme uses adaptive binning to group pixels so that the combined signal-to-noise ratio of each group is above a minimum threshold. Pixels that are already above the threshold are not binned. Thus, the final resolution varies across the image, although at no point is it improved beyond the original resolution in the data.

The algorithm bins pixels together into groups by accreting new pixels to each group according to how close they are to the centroid of the current group. Checks ensure that each time a pixel is added to a group, both the group remains "round" and the signal-to-noise ratio increases. The resulting groups then provide a set of positions (centroids) and mean fluxes that are used as the initial "generators." A further algorithm optimizes the generator configuration based on a centroidal Voronoi tessellation. The final set of generators are the positions of the flux-weighted centroids of each binned group and have the property that each pixel in the original image is assigned to the group corresponding to the nearest generator. Thus, the positions of the generators provide all of the information necessary to recreate the binned image.

Since it can be hard for the human eye to comprehend the binned images created in this way, we have, for the purposes of presentation only, applied a final step of interpolating all of the pixel values from the generators of the Voronoi tessellation using a minimum curvature spline surface (as implemented in IDL version 6.0). In the resulting smooth images, pixels with high signal-to-noise ratio (i.e., unbinned pixels) have very nearly the same value as the original image.

3. THE CIRCUMNUCLEAR STELLAR RING

When the pixel scale of SINFONI is matched to the diffraction limit of the VLT, its field of view is only $\sim$1″. An important step is therefore to understand the larger scale context in which these data reside. To facilitate this, we have used *H*-band data, which trace the stellar light with less bias to recent star formation than optical data, from both the Two Micron All Sky Survey (2MASS) large galaxy atlas (Jarrett et al. 2003) on scales of 2″–100″ and the *HST* archive on scales of 0.″2–10″ (proposal 7172, Rieke). Before analyzing the *HST* F160W image, it was deconvolved using a PSF generated by Tiny Tim 6.2, rotated to the standard orientation and trimmed to 13.″5 on a side. Isophotal fitting (using the `ellipse` task in IRAF) was performed on both these images and the resulting profiles scaled according to their overlapping region. In addition, a bulge-plus-disk model (the parameters of the disk being fixed at the values determined from the large-scale 2MASS data) was fitted to the F160W image, excluding radii smaller than 1.″6, using a χ^2 minimization. This model was then divided into the F160W image in order to investigate the excess continuum emission apparent at radii of 1″–1.″5.

On the largest scales there is an almost perfect exponential profile with a disk scale length of 26.″8 (2.1 kpc) and an axis ratio of 0.4–0.6 (corresponding to an inclination of 55°–65°) at a position angle (P.A.) of roughly −30°. At smaller scales, there is a smooth transition to an $r^{1/4}$ profile with an effective radius of $r_{\rm eff} = 3.''4$ (270 pc), which dominates the emission at radii 2″–9″. This $r_{\rm eff}$ is rather larger than the 2.″6 found by Nelson et al. (2004) from optical data, probably because we have less bias from nuclear star formation and the AGN.

What was previously reported by Chapman et al. (2000) as a possible knotty one-armed spiral is now revealed in Figure 2 as a ring of excess continuum with radius 1.″7 (140 pc). Its axis ratio of 0.6 and P.A. of −30° are consistent with both the large-scale disk and also the circumnuclear molecular gas ring reported by both Schinnerer et al. (2000) and Baker (2000). The

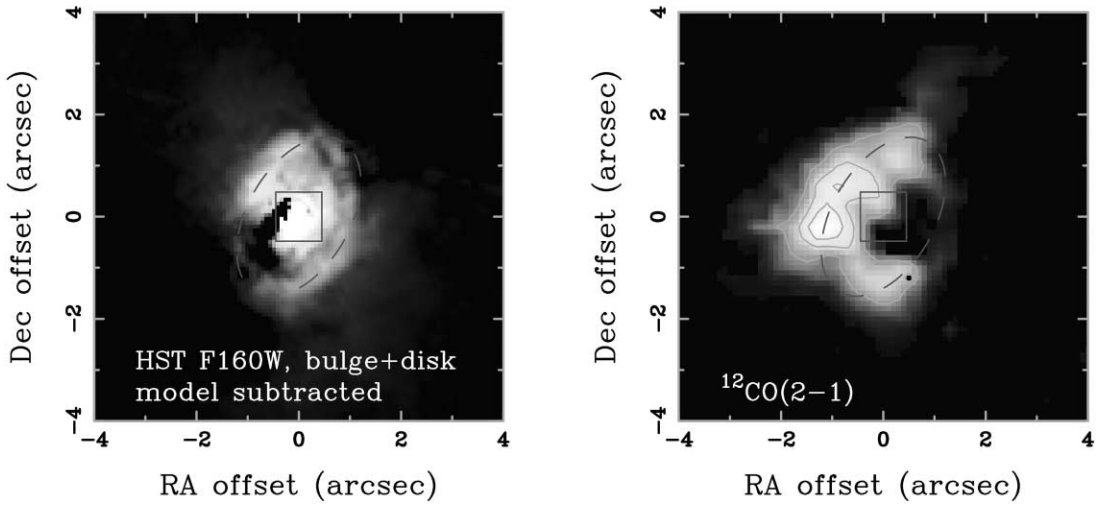

FIG. 2.—*Left: HST* F160W (square root scaling) image after subtracting the bulge-plus-disk model derived from the 2MASS image and the *HST* image at $r > 1\farcs6$. The field of view of SINFONI is shown as a box in the center. The outline of the stellar ring is drawn as a dashed ellipse, with axis ratio 0.6 at a P.A. of $-30°$. *Right*: CO (2–1) molecular gas map from Schinnerer et al. (2000), with contours at 40%, 60%, and 80% of the peak. The same box and ellipse as at left are also marked on this image. North is up and east is to the left. [*See the electronic edition of the Journal for a color version of this figure*.]

kinematics of the CO (2–1) indicates that the gas lies in a disk, and the stellar ring indicates that the stars also lie in a disk, since resonances such as these are features of disk dynamics. The similarity of the loci traced in both cases suggests that the stellar and gas disks are in fact the same. The ring was hypothesized by Schinnerer et al. (2000) to be at the location of an inner Lindblad resonance (ILR) associated with a secondary inner bar on scales smaller than $20''$, which is itself the ILR for the primary bar. Evidence for such a secondary bar was presented by Baker (2000), who noted elongated molecular structures along the major axis at radii of $10''$–$15''$, which he suggests may be concentrations of gas at the leading edges of a bar. However, he cautions that the velocities are different from those expected for gas inflow along the bar.

The $1''$ field of view of SINFONI lies entirely inside the 140 pc ring, as indicated in Figure 2. Its view is presented in Figure 3, where we show images of the 2.1 μm continuum, the stellar continuum measured from the CO 2–0 absorption band head, the 2.12 μm H_2 1–0 $S(1)$ line, the 2.17 μm Brγ line, and the coronal [Ca VIII] line at 2.32 μm. Fluxes and flux densities are summarized in Table 1. The corresponding kinematics for the 1–0 $S(1)$ and Brγ lines and the stellar CO 2–0 absorption are shown in Figure 4. In the left panels we show the full field that can be measured. In the middle panels we have applied a mask to show only velocities associated with the brightest pixels: those that contribute $\frac{2}{3}$ of the total flux, and hence the bulk of the emitting medium, in the field. Velocity dispersions are shown in the right panels.

4. NUCLEAR STAR FORMATION

There is some evidence in the literature that points to a scenario involving recent vigorous star formation in the nucleus of NGC 3227. Based on an analysis of seeing-limited near-infrared integral field spectroscopy, Schinnerer et al. (2001) argued that there was a 25–50 Myr cluster present, although they could not rule out a much older population. In addition, there is the detection of the 3.3 μm polycyclic aromatic hydrocarbon (PAH) feature in a $0\farcs8 \times 1\farcs7$ slit aperture by Rodríguez-Ardila & Viegas (2003). They reported that the ratio $L_{3.3}/L_{\rm IR} \sim 7 \times 10^{-5}$ is lower than the mean for starbursts but typical of Seyfert 2 galaxies. PAHs have also been detected in AGNs where star formation is also active, perhaps most notably Mrk 231 (Rigopoulou et al. 1999) and NGC 7469 (Mazzarella et al. 1994); Davies et al. (2004a, 2004b) have shown beyond doubt that these galaxies host massive nuclear star formation. In this section we address the questions of the presence and age of a distinct stellar component in the nucleus. We consider evidence from the stellar absorption features (§§ 4.1 and 4.2), the narrow Brγ (§ 4.3), and radio continuum (§ 4.4). Finally, we apply population synthesis models in § 4.5.

4.1. *Late-Type Stars and Stellar Luminosity*

The CO band heads at $\lambda > 2.29$ μm are often used as tracers of star formation in the K band since, once they first appear, late-type stars dominate the near-infrared stellar continuum. Under the assumption either that the equivalent width of the CO 2–0 band head, $W_{\rm CO}$, is independent of stellar population or that the stellar population does not change across the region of interest, the absolute absorption in the band head provides a direct tracer of stellar luminosity. However, given that Förster Schreiber (2000) and others have shown that $W_{\rm CO}$ in individual stars can vary from 0 to 20 Å depending on stellar type (effective temperature), the validity of this assumption is far from clear. Fortunately, there is observational and theoretical evidence that it is valid. Oliva et al. (1995) found very little variation in $W_{\rm CO}$ between elliptical, spiral, and H II galaxies. In addition, star cluster models indicate that for ensembles of stars, $W_{\rm CO}$ is much more stable, reaching a value close to 12 Å once the age of the cluster has exceeded 10 Myr. This is demonstrated in Figure 5, which shows how $W_{\rm CO}$ varies as a function of age for various star formation histories. The data were generated using the population synthesis code STARS (Sternberg 1998; Thornley et al. 2000; Davies et al. 2003, 2005; Sternberg et al. 2003), which calculates the distributions of stars in the Hertzsprung-Russell diagram as a function of age for exponentially decaying star formation rates. Using empirically determined $W_{\rm CO}$ from library spectra (Förster Schreiber 2000), the code then computes the time-dependent $W_{\rm CO}$ for the entire cluster of stars. The code includes the thermally pulsing asymptotic giant branch (TP-AGB) stars, which have a very significant impact on the depth of the absorption features at ages of 0.4–2 Gyr (Förster Schreiber et al. 2003; Maraston

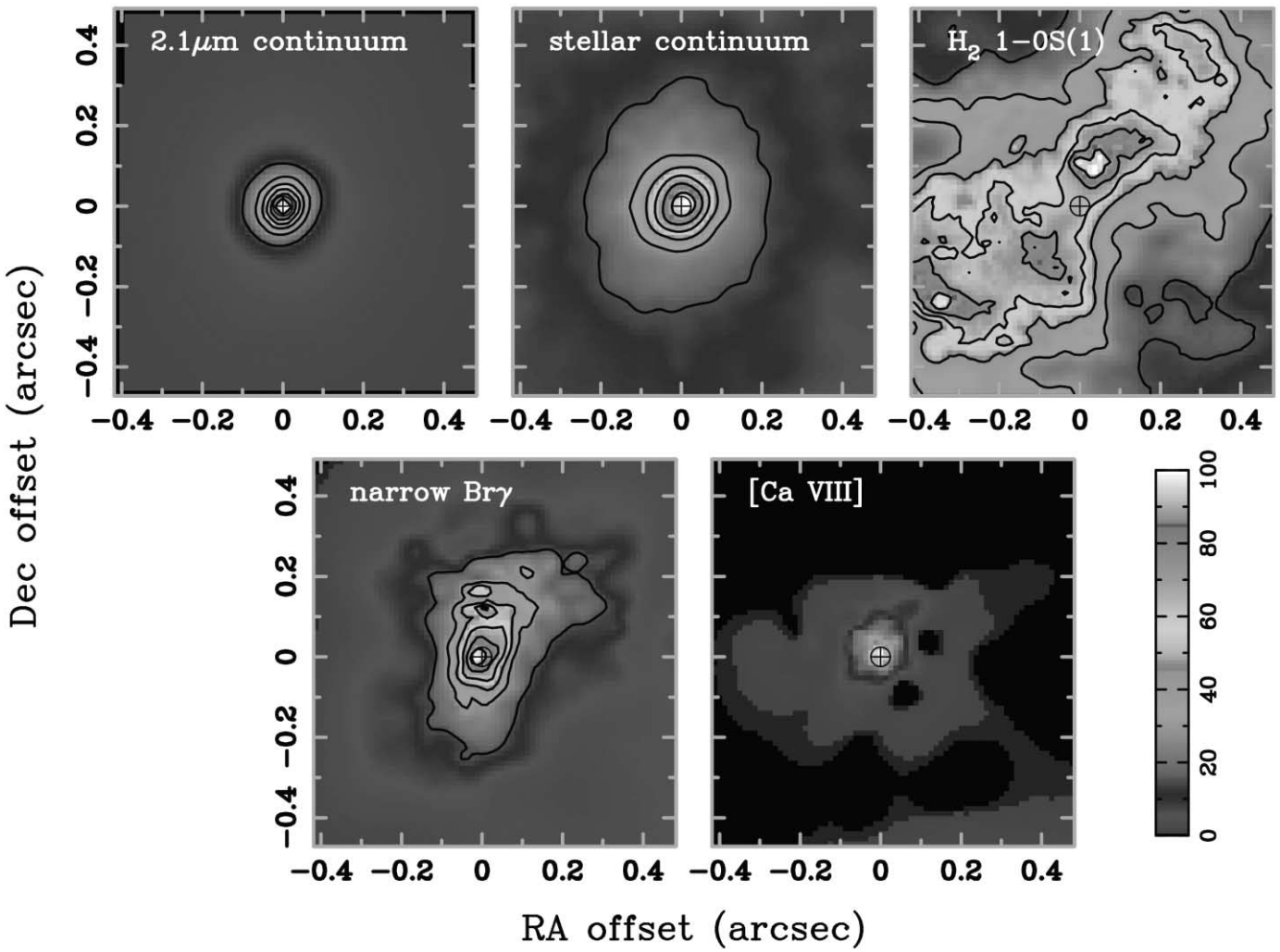

FIG. 3.—Images from the SINFONI data cube showing the primary continuum and emission-line morphologies in the central arcsecond of NGC 3227. In each case, the color scale stretches from 0% to 100% of the peak flux, and contours are spaced equally between 15% and 90% of the peak flux. A crossed circle indicates in each panel the peak of the continuum emission. The maps show, from left to right and top to bottom, 2.1 μm continuum, stellar continuum (derived from the stellar absorption), H_2 1–0 $S(1)$, narrow Brγ, and [Ca VIII]. North is up and east is to the left. [*See the electronic edition of the Journal for a color version of this figure*.]

2005). Throughout this work we adopt a solar metallicity Salpeter initial mass function in the range 1–100 $M_\odot$.

Figure 5 shows that once CO absorption is present, W_{CO} does not deviate from 12 Å by more than 20% except in the special case of instantaneous star formation with an age of less than 15 Myr. This insensitivity of W_{CO} to star formation history means that, although it cannot differentiate between young and old stellar populations, it can be used to distinguish the stellar and nonstellar continuum and to trace the total stellar luminosity profile. The observed $W_{CO} = 3.6$ Å (measured in the bandpass prescribed by Förster Schreiber 2000) implies a mean dilution (i.e., ratio of total continuum to stellar continuum) in a 0.″8 aperture of 3.3 at 2.3 μm. The average dilution over the whole K band will be less: as small as 2.3 if the hottest dust associated with the AGN is at a typical temperature of 500 K within this aperture (or hotter but also reddened). We have adopted an intermediate value of 2.8 corresponding to a characteristic temperature of 1000 K. Within the aperture, we find a K-band magnitude of 10.28 (a little brighter than that given by Schinnerer et al. [2001], perhaps due to their lower resolution or because of the wings often associated with the PSF of shift-and-add data), which implies a stellar magnitude of 11.4 or equivalently a 1.9–2.5 μm luminosity of $\log (L_K/L_\odot) = 7.8$.

This luminosity includes both a possibly young population and the old bulge population. Fortunately, the respective contributions from these two components can be disentangled, as the top panel of Figure 6 shows. This figure includes data at different scales from various sources, all of which have pros and cons: 2MASS H band covers the largest scales but cannot probe scales less than 2″–3″ due to limited resolution; the *HST* F160W image covers intermediate and small scales at high resolution but cannot probe radii smaller than ~0.″2 due to the bright point source associated with the AGN; the SINFONI total K-band continuum covers the central arcsecond at high spatial resolution but is limited by the AGN at radii less than ~0.″05; the SINFONI stellar K-band continuum probes the very smallest scales without being affected by the AGN but is noisier (see Fig. 3). The large-scale disk and bulge models discussed in § 3 reveal an excess of emission at radii less than 0.″5 that increases to become very significant closer than 0.″2 from the center. Presumably this excess is associated with the recent star formation that is also the origin of the narrow Brγ flux. It accounts for 60% of the continuum in a 0.″8 aperture. Hence, the luminosity of the young stellar population is $\log (L_K/L_\odot) = 7.6$.

When compared to the luminosities of star clusters predicted by STARS (e.g., see Davies et al. 2003) or to individual clusters

TABLE 1
Measured Fluxes and Flux Densities for NGC 3227

Item	Measurement[a]	Unit
H_2 1–0 $S(1)$	10.9[b]	10^{-18} W m^{-2}
Narrow Brγ	4.6[b,c]	10^{-18} W m^{-2}
Broad Brγ	42[b]	10^{-18} W m^{-2}
[Ca VIII]	1.5[b]	10^{-18} W m^{-2}
Total K-band continuum	32	10^{-15} W m^{-2} μm^{-1}
W_{CO}	3.6[d]	Å
Young stellar K-band continuum	7.0[e]	10^{-15} W m^{-2} μm^{-1}
Old stellar K-band continuum	4.5[e]	10^{-15} W m^{-2} μm^{-1}

[a] All measurements are given for a 0.″8 aperture centered on the continuum peak.

[b] Uncertainties are approximately 0.3×10^{-18} W m^{-2} (3 times larger for the broad Brγ) and are dominated by calibration and from the stellar continuum features.

[c] We estimate that 25% originates in the narrow-line region and 75% from star formation, yielding the number of ionizing photons from young stars to be $\log Q_{Lyc} = 51.93$.

[d] The dilution at 2.3 μm implied by W_{CO} is greater than the mean dilution over the K band, which is centered at 2.18 μm.

[e] Assuming a dilution over the K band of 2.8; the uncertainty in this corresponds to no more than 20% uncertainty in the stellar continuum flux density. The division between young and old populations is based on the bulge and excess continua as shown in Fig. 6.

in other nearby galaxies, this suggests a very significant (probably young) stellar component within 30 pc of the AGN.

4.2. *Nuclear Stellar Luminosity Profile*

The 2.1 μm continuum (similar to a broadband K image) is dominated by the nonstellar continuum associated with the AGN and is barely resolved, with an FWHM of 0.″10 (cf. the resolution of 0.″085). On the other hand, a simple size measurement of the stellar continuum yields an FWHM of 0.″17, indicating that the nuclear stellar component is easily resolved, having an intrinsic size scale of $\sim$12 pc.

The axis ratio of 0.8 and P.A. of -10° evident in the outer isophotes of the total stellar distribution, and also apparent in the faintest levels of the 2.1 μm image, differ only slightly from those of the 140 pc scale ring. This can be seen in Figure 6: from radii of 10″ where the bulge begins to dominate down to a scale of 2″, the ellipticity of the isophotes decreases; however, as measured in the *HST* F160W data, as well as the SINFONI continuum and stellar band head data, it increases again briefly at both the 1.″7 radius of the ring and also radii 0.″2–0.″5. The stellar kinematics (Fig. 4) shows ordered rotation, albeit with a very large velocity dispersion, at a P.A. of -30° to -45°.

It may be, as appears to be the case in NGC 7469 (Davies et al. 2004a), that the nuclear stellar cluster is triaxial, leading to an offset between the major (isophotal) axis and the kinematic axis. A triaxial potential could conceivably arise in a situation where a nested bar, perhaps associated with the 140 pc ring, is dynamically heated and forms a mini-pseudobulge (Kormendy & Kennicutt 2004). The timescale for such heating is of the order of 10^9 yr for kiloparsec-scale bulges and presumably shorter for nested bars where the pattern speed is faster and significant energy may be injected by either star formation or the AGN. If the heating is due to buckling instability, then it will result in the bar becoming weaker and more centrally compact (Raha et al. 1991), at least qualitatively consistent with what we are seeing here.

However, in interpreting the stellar data one needs to bear in mind that it comprises similar contributions from the bulge and the nuclear component, the observed properties being the combination of these two components. As discussed above, the top panel of Figure 6 disentangles these, and the excess emission revealed is drawn in more detail in Figure 7. At radii 0.″5 the data show a clear break at about 0.″15 characterized by a change in the radial luminosity gradient that is independent of the underlying bulge light (extrapolated from radii 2″–10″ and marked by a dashed line). The profile of the excess can be fitted by an $r^{1/4}$ profile whose effective radius r_{eff} changes at 0.″10–0.″15. However, the two radii are $r_{e1} = 0.''25$ and $r_{e2} = 8.''2$, which are rather larger than the size scales over which the respective regions extend, leading to some doubt about whether they are physically meaningful fits. On the other hand, under the assumption that the excess continuum arises in a disk, it can be fitted equally well by an exponential whose scale length r_d (note that disk scale length is related to effective radius by $r_d = r_{eff}/1.68$) changes at a radius of 0.″11. At smaller radii $r_{d1} = 0.''037$, while at larger radii $r_{d2} = 0.''38$.

In summary, the radial profile and rotational signature suggest a disklike distribution for the nuclear component. On the other hand, the high dispersion and isophotal position angle (although both are biased by the bulge component) indicate a thicker, more spheroidal or even triaxial geometry. Taken together, these results suggest that a thickened disk is the appropriate interpretation for the nuclear stellar light.

4.3. *Ionized Gas and Young Stars*

The Brγ map in the right panel of Figure 3 shows only the narrow (FWHM 200–300 km s^{-1}) component of the line, achieved by fitting out the broad ($\sim$3000 km s^{-1}) component. The resulting emission is resolved along all position angles. The crucial question here is whether the bulk of the Brγ originates from an outflow in the narrow-line region (NLR) or from OB stars. On scales of 1″–7″ the [O III] emission is extended on position angles of 15°–30° (Mundell et al. 1995; Schmitt & Kinney 1996), roughly along the galaxy's minor axis. However, Schmitt & Kinney (1996) also note a knot of emission $\sim$0.″25 from the nucleus that they suggested could be associated with the double-peaked radio continuum source in Mundell et al. (1995). Indeed, approximately 0.″2 north and south of the nucleus, the dispersion of the Brγ line is much larger than elsewhere, which could be indicative that these features are related and originate in the NLR. On the other hand, both the morphology and primary velocity gradient of the Brγ are oriented to the northwest, which is strong evidence for a direct relation to the stars and molecular gas. A quantitative discrimination can be made by assigning emission with a dispersion greater than 150 km s^{-1} to the NLR, and the rest (which lies along the major axis) to star formation. We find that $\sim$75% of the Brγ flux most probably originates in star formation. Section 4.5 and Figure 8 address the consequences on our starburst models of the uncertainty of this conclusion.

4.4. *Radio Continuum and Supernova Remnants*

A map of the 6 cm radio continuum at a resolution of $0.''05 \times 0.''07$, comparable to what we have achieved, was published by Mundell et al. (1995). This showed a 0.″3 long structure, composed of knots of emission, elongated at a P.A. of -10°. In the $0.''14 \times 0.''17$ resolution 18 cm map these features were visible only as a bright compact source and a tail to the north, but an additional bright knot was also apparent 0.″4 to the north. Mundell et al. (1995) suggested that these features might be radio jets, either one or, if the nucleus actually sits between the brightest knots, two sided. However, they noted a number

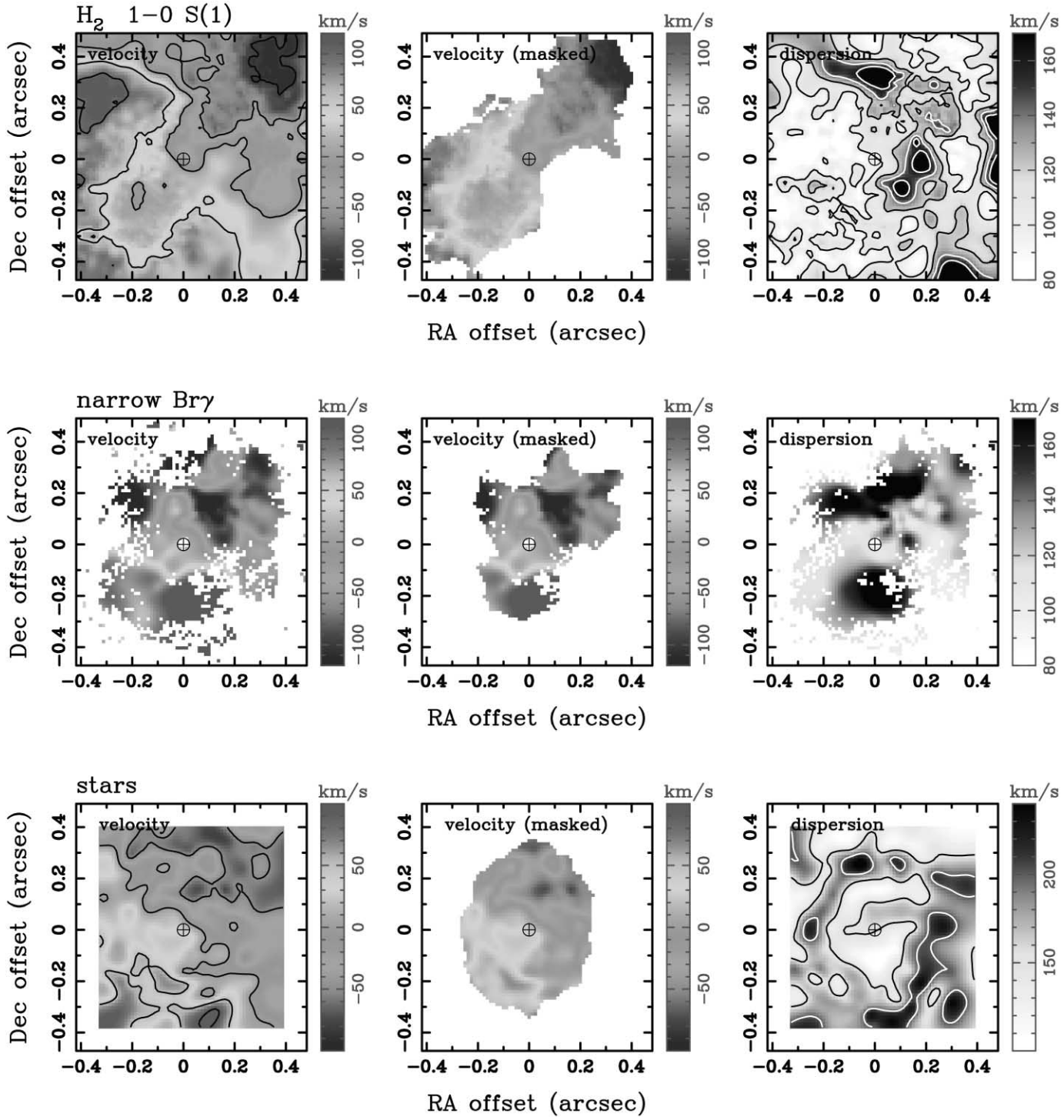

FIG. 4.—Measured kinematics for the gas and stars in the central arcsecond of NGC 3227. *Top*: H_2 1–0 $S(1)$ line; *middle*: narrow component of the Brγ line; *bottom*: stars. *Left*: Velocity field, determined as described in § 2; *middle*: the same velocity field, masked to include only those pixels with higher fluxes: in each case, these pixels make up $\frac{2}{3}$ of the total flux; *right*: dispersion. The maps for emission lines are at a resolution of 0.″085; those for the stars have had additional smoothing and are at an effective resolution of 0.″115. Note that in the line dispersion maps, the data have not been corrected for the instrumental resolution, which corresponds to $\sigma = 30$ km s^{-1}. [*See the electronic edition of the Journal for a color version of this figure.*]

of difficulties with this interpretation: lateral extensions were detected well above the noise level, and the jet orientation differs from that of the NLR, as traced by [O III]. They suggested that as in NGC 4151 (e.g., Pedlar et al. 1993), misalignment may be expected between the radio axis, which lies along the collimation axis of the UV ionization cone, and a density-bounded extended narrow-line region (ENLR). However, they also realized that the line widths of the [O III] are indicative of an NLR rather than an ENLR, and in addition for such a model to apply, the northeast side of the disk would have to be closer and hence the spiral arms would have to be leading rather than trailing. To circumvent these difficulties, they suggested that the radio collimation and [O III] outflow may not be due to the same mechanism.

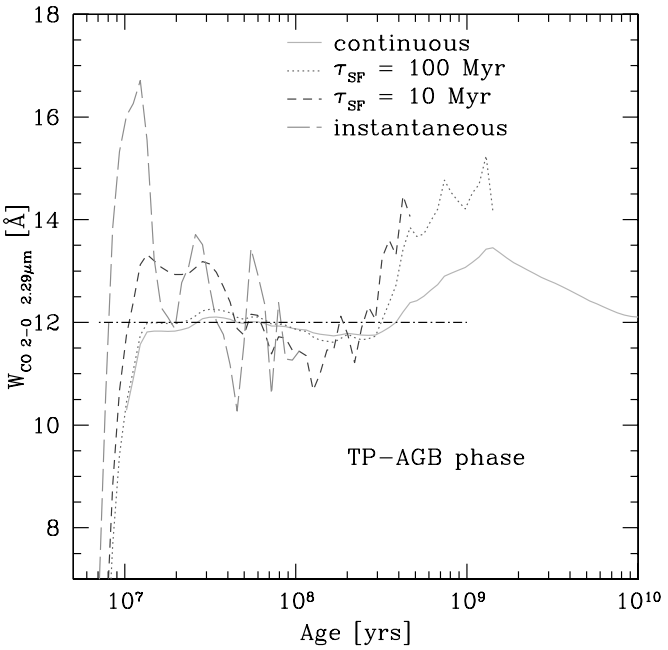

FIG. 5.—Equivalent width of the 2.294 μm CO 2–0 band head as a function of age, calculated using STARS (which includes the TP-AGB stars). Several different star formation histories are shown: instantaneous, a decay time of 10 Myr, a decay time of 100 Myr, and continuous. For each history, data are plotted where the *K*-band luminosity is at least 1/15 of its maximum. This indicates that one expects $W_{CO} \sim 12$ Å for nearly all star-forming scenarios.

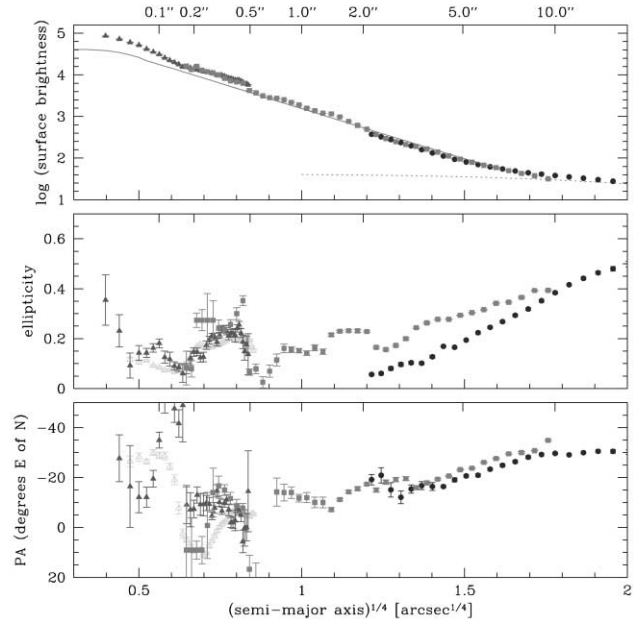

FIG. 6.—Luminosity profile (*top*), ellipticity (*middle*), and P.A. (*bottom*) as functions of radius for NGC 3227. Data from different sources are denoted by circles for 2MASS *H* band, squares for *HST* F160W, filled triangles for the SINFONI stellar *K*-band continuum, and open triangles for the SINFONI total *K*-band continuum. In the top panel, the relative scaling has been adjusted according to the overlapping regions. The dotted line indicates the large-scale disk, the solid line the bulge plus disk. A clear emission excess is apparent in the central arcsecond, associated with changes in ellipticity and position angle. [*See the electronic edition of the Journal for a color version of this figure.*]

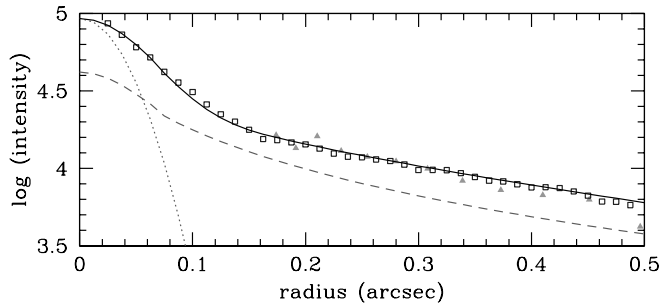

FIG. 7.—Radial profile of the nuclear stellar light. Filled triangles denote *HST* F160W data, and open squares the SINFONI *K*-band stellar continuum. The gray dotted line indicates the spatial resolution by tracing a Gaussian with 0.″085 FWHM. The gray dashed line represents the $r^{1/4}$ bulge fit at 2″–10″ radii extrapolated inward. The solid line indicates a fit to the data including the bulge component and an exponential whose scale length changes at a radius of 0.″11.

These discrepancies cease to be issues (indeed, actually are expected) if instead one attributes the radio continuum to supernova remnants (SNRs). In this scenario, the knotty morphology could arise from the superposition of many SNRs, some of which are perhaps bright enough to be detected as individual radio supernovae. Supporting this, the bright northern knot apparent in the 18 cm map is a result of the low resolution of that map: Figure 9 shows that the same knot seen in a low-resolution 6 cm map breaks up into discrete structures at higher resolution. For such an interpretation, the details of the morphology have no more significance than tracing the locations of these stochastic events.

The flux density of the individual 6 cm knots in NGC 3227 is variable, with the brightest being 1–2 mJy (excluding the extended nuclear knot, which probably comprises many SNRs). This implies luminosities up to $(3-6) \times 10^{19}$ W Hz^{-1}, fully consistent with the range of $(1-1000) \times 10^{19}$ W Hz^{-1} for the peak 6 cm flux density of galactic radio supernovae given by Weiler et al. (2002).

For comparison, in Arp 220, 16 radio supernovae with 18 cm luminosities $(20-60) \times 10^{19}$ W Hz^{-1} (a factor of $\sim$3 lower at 6 cm, assuming a spectral index $\alpha = -1$) were reported by Smith et al. (1998), and for the 24 sources monitored in the nucleus of M82, 6 cm luminosities are in the range $(0.1-10) \times 10^{19}$ W Hz^{-1} (Kronberg et al. 2000). In both of these galaxies, most of the SNRs appear to have varied rather little in flux over, respectively, 5 and 12 yr periods (Rovilos et al. 2005; Kronberg et al. 2000). The flux densities of the knots in NGC 3227 are therefore certainly consistent with their being radio supernovae.

We have superimposed the radio continuum data (naturally weighted, $0.''076 \times 0.''053$ beam size, kindly made available and rereduced by C. Mundell) and SINFONI data, as shown in Figure 9. Since no astrometrical alignment is possible, we have assumed that the brightest 6 cm emission coincides with the peak in the *K*-band stellar continuum, which is justifiable if, as we suspect, the 6 cm emission is due to star formation. For this interpretation, the exact astrometrical alignment is not critical. An alternative alignment could be for the near-infrared nucleus to lie between the two main emission knots seen in the 18 cm map of Mundell et al. (1995). However, this seems unlikely because, as we have shown, the jetlike structure is in fact small spread-out knots seen at low resolution. There is perhaps some correspondence between these off-nuclear 6 cm continuum knots, which tend to lie to the northwest, and the Brγ line, which is also more extended in the same direction. Both of these can be understood in terms of a slight tendency for more, or more recent, star formation there. On the other hand, it is clear that there is

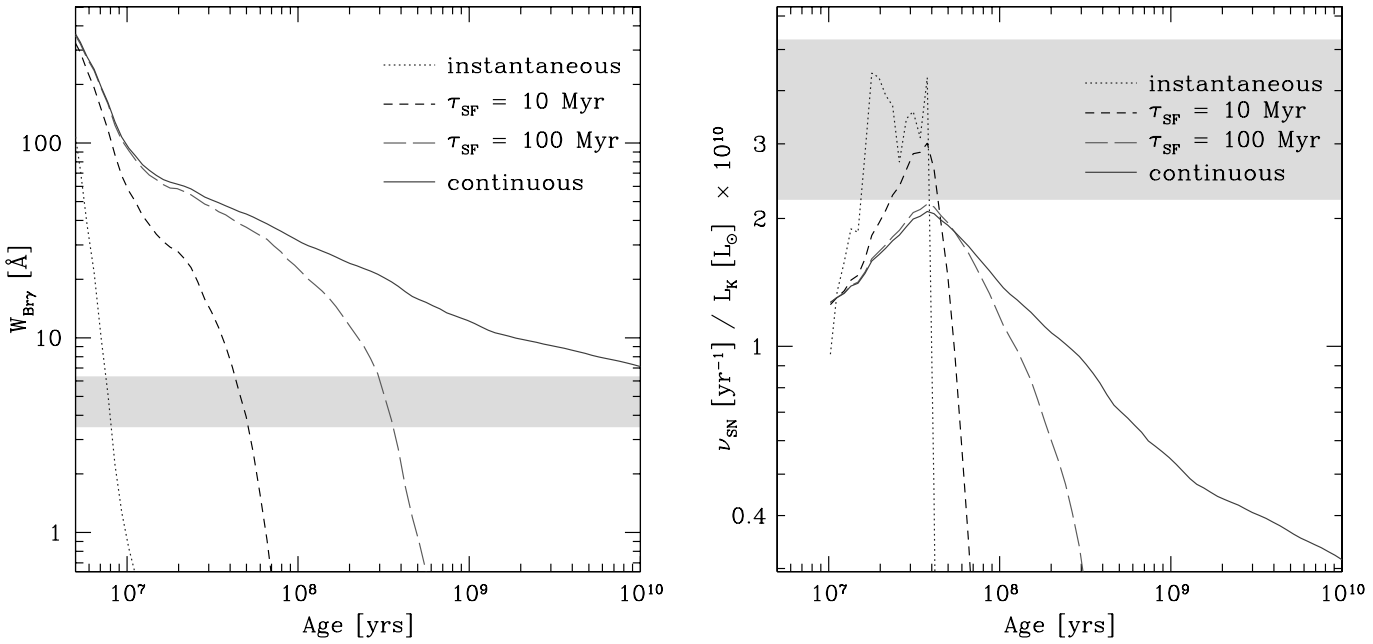

FIG. 8.—Plots of $W_{Br\gamma}$ (*left*) and ν_{SN}/L_K (*right*) as a function of age for four star formation histories. The gray bands indicate the range of the measured ratios, and in both cases only the stellar continuum has been considered. The only scenario that yields a consistent age for both diagnostics is star formation over a timescale of ~10 Myr that occurred ~50 Myr previously.

little one-to-one correspondence between the 6 cm continuum and 1–0 $S(1)$ line.

To estimate the emission within 0.″8, we take two extreme limits: that for the nucleus (i.e., southern component) only, as well as the total, both given by Mundell et al. (1995). We estimate the maximum AGN contribution by measuring the flux in the central 0.″090 (to include the full beam) as no more than 10% of the total. We have made no correction for this. Using the conversion given in Condon (1992) for these 6 and 18 cm flux densities, we estimate the supernova rate to lie within the range 0.008–0.019 yr^{-1}.

4.5. *Star Cluster Models*

The discussion above has yielded two independent diagnostics that can be used to constrain the star formation history in the central arcsecond of NGC 3227. The first is the (classical) equivalent width of Brγ. We use the ratio of the narrow Brγ associated with young stars (i.e., excluding the NLR contribution) to young stellar continuum, thus removing any bias associated with the AGN or bulge. The ratio we adopt is therefore $W_{Br\gamma}$ = 5 Å, with an uncertainty of no more than 1.5 Å. The second is the ratio of the supernova rate to stellar continuum luminosity, which is $10^{10}\nu_{SN}(\mathrm{yr}^{-1})/L_K(L_\odot) = 2.2$–$5.3$. These ratios are presented graphically together with models for various star formation histories in Figure 8, allowing some conclusions to be drawn immediately.

The $W_{Br\gamma}$ is too low for the star formation to be continuous, a result supported by the ν_{SN}/L_K, which is sufficiently large that it permits only young ages. This conclusion is robust even to large uncertainties in the two parameters. In particular, Figure 8 shows

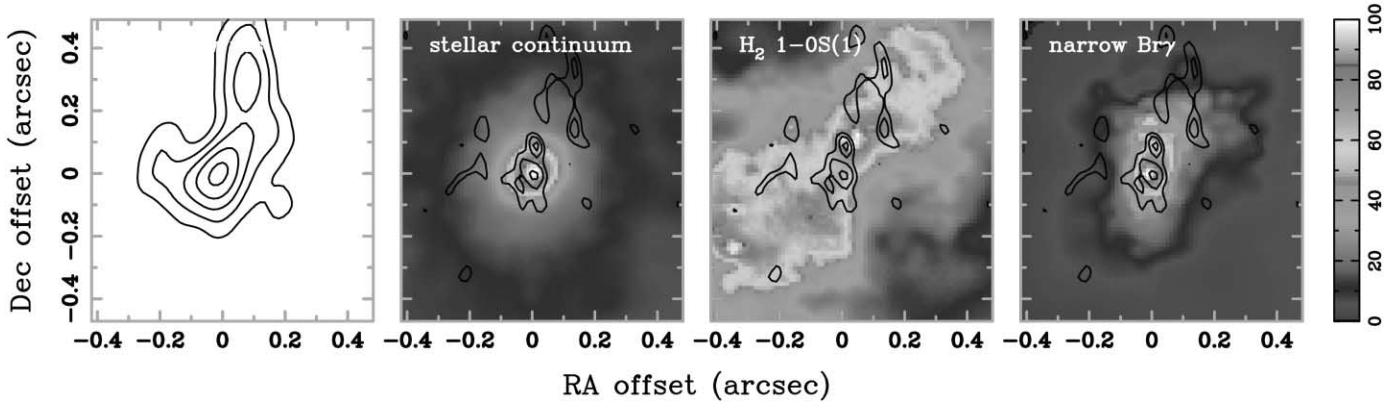

FIG. 9.—Contour plots of the 6 cm radio continuum kindly provided by C. Mundell. *Left panel*: At low resolution [(u, v)-tapered image with beam size 0.″191 × 0.″141], demonstrating that the two blobs seen at 18 cm (Mundell et al. 1995) break up into discrete sources at higher resolution. *Right three panels*: At high resolution (naturally weighted image with beam size 0.″076 × 0.″053). Contour levels are at 2, 3.5, and 5 times the rms noise of 0.37 mJy beam^{-1}. Images on which the contours are superimposed are from Fig. 3. It is not possible to align the data astrometrically. Instead, we have assumed that the brightest 6 cm peak coincides with the peak in the K-band stellar continuum, justifiable under the assumption that the radio continuum is due to star formation. This alignment is not critical to the interpretation. North is up and east is to the left. [*See the electronic edition of the Journal for a color version of this figure.*]

TABLE 2
Derived Properties for the Central 0.″8 of NGC 3227

Item	Measurement[a]	Unit
$\log(L_K/L_\odot)$ (stellar)	7.8	...
$M_{\rm gas}$	$(2–20) \times 10^7$	$M_\odot$
Young stellar component:		
$\log(L_K/L_\odot)$	7.6	...
$\log(L_{\rm bol}/L_\odot)$	9.5	...
Initial star formation rate	3	$M_\odot$ yr^{-1}
Current star formation rate	0.05	$M_\odot$ yr^{-1}
Age	40	Myr
e-folding decay time	10	Myr
M_*/L_K	0.5	$M_\odot\ L_\odot^{-1}$
M_*	2×10^7	$M_\odot$

[a] All measurements apply to a 0.″8 aperture centered on the continuum peak.

that the conclusion is valid even if either $W_{\rm Br\gamma}$ is overestimated by insufficient correction for the NLR contribution or $\nu_{\rm SN}/L_K$ is overestimated by not correcting for a possible AGN component. Thus, any star formation that did occur has now ceased. On the other hand, because there are already SNRs, at least 10 Myr must have elapsed since star formation began. Thus, an instantaneous burst is ruled out because of the steepness with which $W_{\rm Br\gamma}$ falls. For the intermediate histories, the age of the star formation is strongly constrained by $\nu_{\rm SN}/L_K$, even if the ratio itself is rather uncertain, to be at most 50 Myr. Even if one allows the uncertainty in the conversion from continuum flux density to supernova rate, it would be hard to reach ages greater than 100 Myr. With this in mind, the low $W_{\rm Br\gamma}$ requires a short but finite burst timescale. The best model is for a burst with an e-folding decay time of 10 Myr that began 40 Myr ago. However, we emphasize that a unique match is not the aim of this modeling; the important result is that the star formation is very young and that the active episode lasted for a finite time but is now finished. This is an interesting result, begging the following questions: Since stars form in cold quiescent environments, how did such intense star formation occur in this environment, which is clearly extremely turbulent [as evidenced by the 1–0 $S(1)$ morphology in Fig. 3 and the velocity dispersion of 100–125 km s^{-1}, which is significantly higher than the rotational velocity of 50–100 km s^{-1}]? Once started, what is it that caused the star formation to cease while the gas is still so plentiful? We address these questions in § 6.

The properties we find for the star formation scenario given above for the measurements in a 0.″8 aperture are summarized in Table 2. The star formation has an initial rate of 3 $M_\odot$ yr^{-1} and a current rate of 0.05 $M_\odot$ yr^{-1}. The current mass-to–K-band light ratio is $M/L_K = 0.5\ M_\odot\ L_\odot^{-1}$, where the mass of $2.0 \times 10^7\ M_\odot$ refers to the current live stars rather than the total gas consumed during the active phase, which is almost 50% greater. Remarkably, the current bolometric luminosity attributable to these stars is $\log(L_{\rm bol}/L_\odot) = 9.5$. This is a crucial result, since it implies that the extinction to the stars cannot be very great.

Figure 7 shows that within the central 0.″8 we discuss above, the intensity increases dramatically at $r < 0.''11$ (9 pc). Within this smaller radius, the star formation models show that the mean stellar mass surface density is $3 \times 10^4\ M_\odot$ pc^{-2}. Averaged over the last 40 Myr (i.e., since the burst began), the mean absolute star formation rate is only 0.13 $M_\odot$ yr^{-1}, but the rate per unit area has been phenomenally high: typically 500 $M_\odot$ yr^{-1} kpc^{-2} and reaching rates 10 times higher in intensity at its peak when it was active This is more like what one typically expects of ultraluminous galaxies and suggests that during active star-forming phases, which appear to last for similar timescales of a few times 10^7 yr, the local (i.e., $\lesssim$10–100 pc) environment around AGNs is comparable to that in ultraluminous infrared galaxies.

4.6. *Extinction*

So far we have implicitly assumed that there is negligible extinction, and already we account for 20% of the bolometric (i.e., 0.3–1000 μm) luminosity of the entire galaxy.

If we take the reasonable stance that the gas and stars are mixed (rather than the gas lying in front of the stars as a foreground screen), then when considering the effects of extinction we should use the appropriate mixed model for which the reduction in observed intensity depends on optical depth through the gas and stars as $I/I_0 = (1 - e^{-\tau_{\rm mix}})/\tau_{\rm mix}$. The usual scaling of the optical depth with wavelength $\tau_K = 0.1\tau_V$ still applies, as does the definition of the reddening $A_\lambda = -2.5 \log(I_\lambda/I_{\lambda 0})$. This means that in contrast to the screen model for which $A_\lambda = 1.09\tau_\lambda$, in the mixed model a modest observable reddening can hide the existence of a very large optical depth of gas and dust since $A_\lambda = 2.5 \log \tau_\lambda$ (for $\tau_\lambda \gtrsim 3$). Note, however, that often extinctions for mixed models are given as a sort of "screen equivalent," giving rise to very large values. To avoid this confusion when discussing flux attenuation, in the remainder of this paper we refer to the more physical quantity optical depth τ_λ rather than the observationally motivated extinction A_λ.

As an illustration, a reasonable optical depth of $\tau_V = 10$ for the mixed model would mean that 90% of the UV and optical light, which dominates the spectral energy distribution, would be reradiated in the mid- to far-infrared. In addition, the scale of the starburst would increase since L_K becomes 1.6 times that observed. Thus, the net effect is that the bolometric luminosity of the starburst would be $L_{\rm bol}/L_\odot = 9.7$ and account for approximately 50% of the infrared (8–1000 μm) luminosity (although none of the optical luminosity). Similarly, one can derive the maximum possible mixed model optical depth, for which the starburst accounts for all of the 8–1000 μm luminosity, to be $\tau_V = 26$. This is a strong constraint on the extinction, and we return to this point in § 6.3.

Do we see evidence for any extinction? The F160W image in Figure 2 highlights a curious feature in the central arcsecond. In addition to the bright point source associated with the AGN, there is a strong contrast in brightness between the southwest and northeast sides of the nucleus, corresponding to near and far sides, respectively, of the galactic disk for the orientation above. This is reflected in the corresponding spectra extracted from the SINFONI data cube, as Figure 10 shows. The nuclear spectrum is characterized by a flat slope and shallow CO band heads indicative of dilution by hot dust and perhaps also extinction. The spectrum to the southwest has a bluer slope and deeper band heads, both consistent with pure unreddened stellar light. In contrast, the northeastern spectrum has deep band heads but a flatter slope, suggesting that it is reddened (but not diluted). A differential extinction (screen model) of $A_K = 1.2$ would produce the observed change in spectral slope. On the other hand, for the mixed model, any (largish) extinction is possible. For a mixed model, the differential extinction between 2.1 and 2.3 μm saturates at this level and cannot make the slope redder. One might conclude that while the star formation on the southwest side might be predominantly unobscured, that on the northeast side is probably mixed with considerable dust and gas. Conversely on larger scales of 1″–2″, Chapman et al. (2000) found

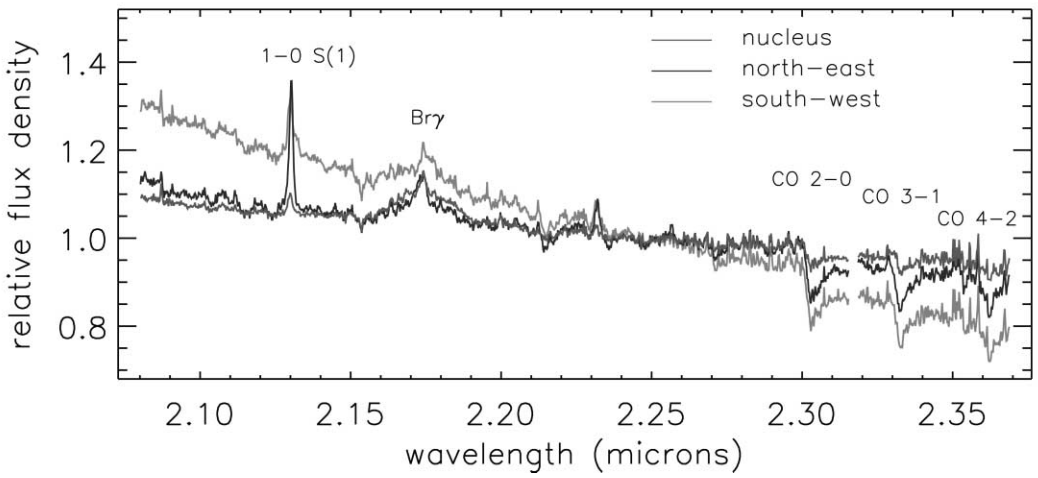

FIG. 10.—Spectra extracted from the SINFONI data cube in 0.″25 apertures centered on the nucleus (*bottom line on the left side of the figure*), 0.″25 to the northeast (*middle line on the left side of the figure*), and 0.″25 to the southwest (*top line on the left side of the figure*). All spectra are normalized at 2.25 μm. The effect of dilution on the CO band heads is clearly seen in the nuclear spectrum. [*See the electronic edition of the Journal for a color version of this figure*.]

evidence from optical and infrared color maps for greater extinction on the southwest side.

5. STELLAR KINEMATICS AND THE BLACK HOLE MASS

None of the velocity fields in Figure 4 show evidence for the extreme warp proposed by Schinnerer et al. (2000) based on their 0.″6 resolution CO (2–1) data. The existence of a small warp would not be surprising since very high spatial resolution mapping of masers indicates that on small spatial scales warps may be common in galactic nuclei, for example, NGC 4258 (Herrnstein et al. 1996), NGC 1068 (Greenhill et al. 1996), and Circinus (Greenhill et al. 2003). The reason for the apparent discrepancy is that Schinnerer et al. (2000) had interpreted the high gas dispersion as spatially unresolved rotation or inflow, whereas our data show that the gas dispersion $\sigma_{\rm gas} \sim 120$ km s^{-1} is intrinsically high. This is not very different from the stellar dispersion σ_* of 140–160 km s^{-1}, which indicates that random motions rather than ordered rotation dominate the kinematics of the stars. As indicated above, the observed data are the superposition of kinematics of the bulge and nuclear component, and this may be responsible for some of the unusual characteristics of the dispersion most easily seen in Figure 11. This shows that σ_* is constant at larger radii (out to our radial limit) but decreases at 0.″1–0.″2. This is exactly the radius at which Figure 7 shows an increase in the intensity of the stellar light from the nuclear component. It is therefore possible that at larger radii the observable σ_* is dominated by the older bulge, but at smaller radii σ_* is more strongly affected by the stars in the nuclear region. If this is indeed the case, then the subsequent increase of σ_* very close to the nucleus could be due to the influence of the black hole.

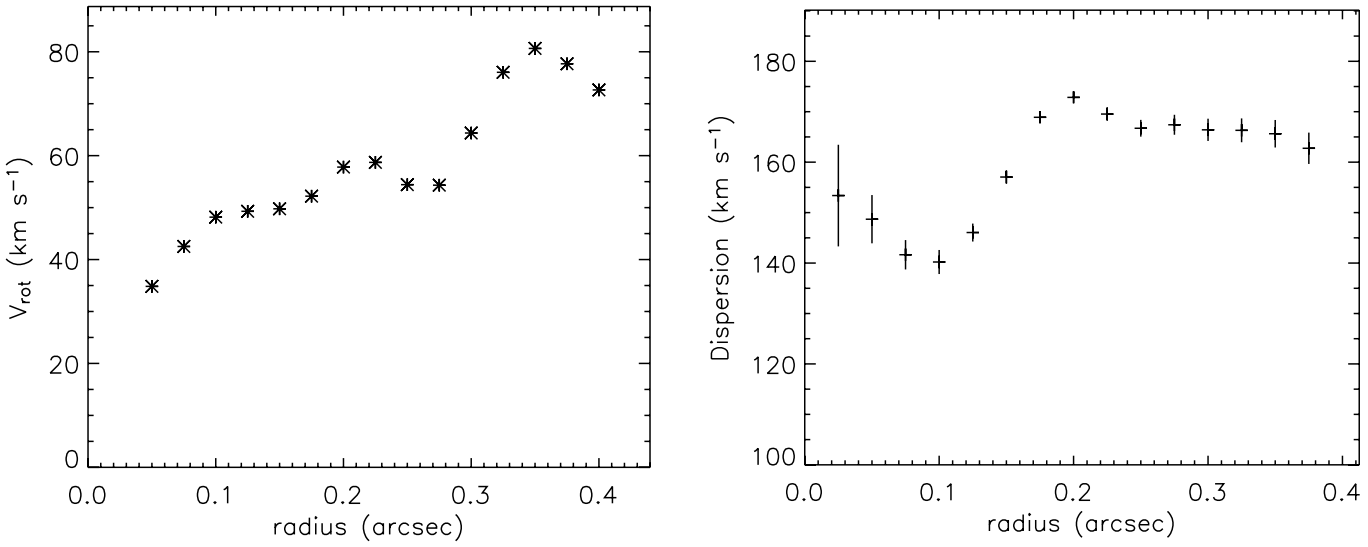

FIG. 11.—*Left*: Stellar rotation curve (found using the commonly employed tilted ring model put forward by Begeman 1989); *right*: azimuthally averaged radial profile of the stellar dispersion. In both cases a fixed inclination of 55° at a P.A. of 135° was adopted. The velocity increases steadily to ~80 km s^{-1} at 0.″4. The dispersion of 160–170 km s^{-1} drops quickly to 140 km s^{-1} inside a radius of 0.″2 , perhaps because of the increasing predominance of the young stars, and then begins to increase slowly at the smallest radii, perhaps due to the dynamical impact of the black hole.

To test whether the behavior of σ_* is consistent with what one might expect from the nuclear star cluster and black hole, we have made a simple dynamical model. This is realized as an edge-on thin disk for which the mass profile follows the luminosity profile given in Figure 7 and accounts for both the gas and stellar mass. For this purpose, we have ignored the luminosity from the large-scale bulge (denoted by the dashed line in the figure). To simulate the random motions that we have shown are important, we have convolved the model spectrally with a Gaussian having $\sigma = 120\,\mathrm{km\,s^{-1}}$. The model is then convolved with the effective spatial resolution and finally "observed" (for more details of how the model is generated see Davies et al. 2004a, 2004b). Although this model does not represent the true three-dimensional mass distribution, the radial distribution is correct and hence it is able to provide a first estimate of the way in which the velocity dispersion changes with radius. In addition, it can, at least quantitatively, show how the rotation velocity is expected to change with radius. The first conclusion is that the increase in σ_* at $r < 0\farcs1$ is indeed consistent with the nuclear mass distribution and presence of a black hole with mass of order $2 \times 10^7\,M_\odot$. The second conclusion confirms that, as expected, the system cannot be rotationally supported: the measured velocities in Figure 11 are only 60%–65% of those needed for this. Nevertheless, the steep increase in $V_{\rm rot}$ out to $r = 0\farcs1$ and subsequent more gradual rise do match the shape of the model rotation curve.

In order to understand the kinematic behavior more fully and to determine $M_{\rm BH}$ from the stellar kinematics, we have constructed an appropriate Schwarzschild orbit superposition model, which is described and discussed below. NGC 3227 is a good candidate for such an analysis because it has already been the focus of other efforts to derive $M_{\rm BH}$. These include reverberation mapping, which yielded $(4.2 \pm 2.1) \times 10^7\,M_\odot$ (Peterson et al. 2004); X-ray variability measurements, giving $2.2 \times 10^7\,M_\odot$ (Nikolajuk et al. 2004); and the $M_{\rm BH}$-σ_* relation itself, leading to $(3.6 \pm 1.4) \times 10^7\,M_\odot$ (Nelson et al. 2004). Based on these masses and the velocity dispersion of 136 km s^{-1} measured by Nelson et al. (2004), one can estimate the "radius of influence" of the black hole to be $r_g \sim GM_{\rm BH}/\sigma^2 \sim 8$ pc. Hence, the black hole dominates the dynamics in the central 16 pc, a region that is easily resolved at our 7 pc FWHM spatial resolution.

5.1. *Schwarzschild Modeling*

Schwarzschild's (1979) orbit superposition technique has become the standard tool for deriving $M_{\rm BH}$ from the kinematics of the surrounding stellar spheroid. The procedure commonly involves four steps: (1) the photometry is deprojected to get the luminosity distribution ν of the stars; (2) a gravitational potential is constructed from trial values for the stellar mass-to-light ratio Υ and the black hole mass $M_{\rm BH}$; (3) thousands of orbits in this potential are combined to match the stellar luminosity distribution and the kinematical constraints; (4) Υ and $M_{\rm BH}$ are systematically varied to find the optimal solution in a χ^2 sense. The specific implementation of the method we use here is detailed in Thomas et al. (2004). The program is based on the code of the Nuker team (D. Richstone et al. 2006, in preparation) that has been used to measure black hole masses in numerous elliptical galaxies (Gebhardt et al. 2003), including Cen A (Silge et al. 2005). We apply these models here with the aim of constraining the black hole mass rather than necessarily deriving uniquely the kinematic structure of the entire system.

The validity of our models rests on two major assumptions: that the central region of NGC 3227 is (1) stationary and (2) axisymmetric. The first assumption is difficult to verify independently. From the quality of our fits to the data (see Fig. 16) we can, however, conclude that, within the uncertainties, this assumption is consistent with the data. To which degree the second assumption holds for NGC 3227 can be estimated from variations in the kinematics from quadrant to quadrant (see § 5.1.2). Providing means to measure such variations is one of the advantages of using a full two-dimensional field of view as we do here. The other advantage is that such data constrain the kinematics of all kinds of orbits that are needed to map the system.

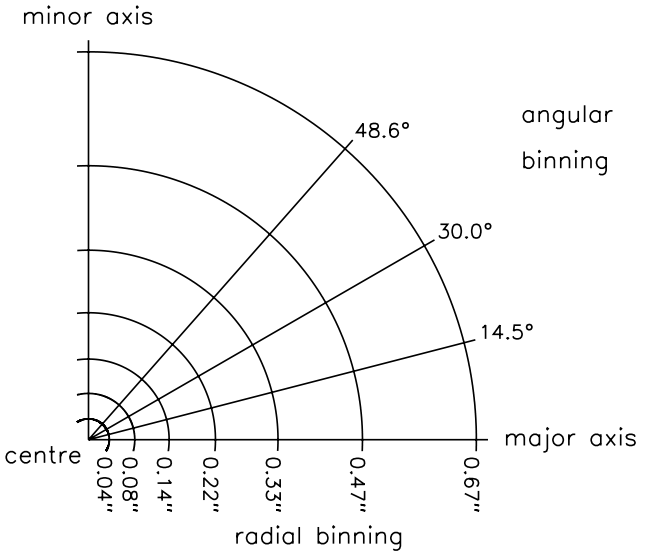

FIG. 12.—Radial and angular binning scheme used as input for the Schwarzschild orbit superposition modeling. The same arrangement was repeated for each of the four quadrants. The total number of bins (32×4) is well matched to the number of independent data points, given the spatial resolution of 0.″085 and the 0.″93 field of view.

The present models for NGC 3227 are calculated on a grid with 7 radial and 4 angular bins in each quadrant (Fig. 12), giving a total that is comparable to the number of spatially independent regions in the data. The binning resolution is matched to sample more frequently the regions where the greatest variations in V and σ are expected to lie. For each mass model about 2×3300 orbits are tracked (the initial factor 2 due to the inclusion of a prograde and retrograde version of each orbit), which, based on the criterion in Richstone et al. (2004), is easily sufficient.

We now discuss how the observations are prepared for the models.

5.1.1. *Photometry*

As we have shown, the luminosity distribution comprises two parts: the bulge and the nuclear star-forming region.

The bulge, which has an $r^{1/4}$ profile with an effective radius in the K band of 3.″4, contributes 40% of the nuclear K-band luminosity and outside of this immediate region dominates the K-band luminosity to a radius of 9″. Due to its high mass-to-light ratio (M/L_K), it has an important effect on the model. We are unable to constrain its M/L_K ratio directly, but from a literature search Förster Schreiber et al. (2003) found that empirical determinations lie in the range 10–30 $M_\odot\,L_\odot^{-1}$, similar to those predicted by population synthesis models for old (∼10 Gyr) populations.

The nuclear star-forming region contributes 60% of the nuclear K-band luminosity and has a K-band luminosity profile that is well matched by an exponential profile with a change in scale length from 0.″037 to 0.″38 at 0.″11. Its M/L_K ratio is well constrained via population synthesis models to be 0.5 $M_\odot\,L_\odot^{-1}$.

However, its mass could be dwarfed by that of the molecular gas that lies in the same region and that we assume has the same radial profile. The gas clearly contributes significantly to the gravitational potential and implies that the effective M/L_K ratio should probably be rather higher.

As a novel feature of our models, and due to the uncertainties in the M/L_K ratios, we allow the contributions of the two components to the total (stellar) mass profile $\rho_{\rm star}$ to be varied independently. To this end the nucleus and the bulge are deprojected separately using the program of Magorrian (1999) and combined via

$$\rho_{\rm star} \equiv \Upsilon_{\rm nuc}\nu_{\rm nuc} + \Upsilon_{\rm bul}\nu_{\rm bul}. \quad (1)$$

Thereby, the (K band) mass-to-light ratios $\Upsilon_{\rm nuc}$ and $\Upsilon_{\rm bul}$ of nucleus and bulge ($\nu_{\rm nuc}$ and $\nu_{\rm bul}$ are the corresponding deprojections) are assumed to be constant with radius. We set the ellipticity of nucleus and bulge $\epsilon_{\rm nuc} \equiv \epsilon_{\rm bul} = 0.3$. The inclination can be varied arbitrarily but must be equal for both components (to ensure axisymmetry).

5.1.2. *Kinematics*

The velocity and dispersion were found for each radial and angular bin shown in Figure 12, by calculating the mean of all spatial pixels within each bin, weighted according to the uncertainty of each measurement. The uncertainties were combined in a similar fashion to estimate the standard error of these means. The position angle that defines the major axis, and hence the orientation of the bins, is relatively well constrained. We have shown that on scales of 140 pc and more, there is no doubt that it is at -30°. On the scales we consider here, less than 50 pc, the data indicate a preference toward -45°. We have therefore adopted -40°, which is sufficiently close to both limits that, given the size of the angular bins, the small uncertainty will have no impact on the resulting model. As input to the orbit models binned line profiles are generated from the measured kinematical parameters (see, e.g., Thomas et al. 2005). Uncertainties in these parameters are propagated on the basis of Monte Carlo simulations.

The stellar dynamical determination of the black hole mass for NGC 3227 suffers from two difficulties: First, due to the constraints of signal-to-noise ratio, it was not possible to derive the Hermite terms h_3 and h_4 from the spectra in any meaningful way. These higher order moments, however, contain important information about the distribution of stellar orbits (Dehnen & Gerhard 1993). Unfortunately, due to the so-called "mass-anisotropy degeneracy," uncertainties in the orbit distribution directly translate into uncertainties in the derived black hole masses. Anyway, in order not to bias our models, we allow for a rather large range of h_3 and h_4 by using $h_3 = h_4 = 0 \pm 0.1$ when deriving the line profiles and their uncertainties.

The second limitation originates in the quadrant-to-quadrant variations of v and σ, which are generally larger than the statistical errors. This indicates that the modeled region is not exactly axisymmetric. When averaging the kinematics from the four quadrants, these variations are taken into account in the error bars.

In summary, the assigned error bars to the kinematical input parameters are rather large and mostly reflect (1) systematic uncertainties related to central deviations from axisymmetry and (2) our ignorance about the higher order Gauss-Hermite moments.

5.2. *The Black Hole Mass of NGC 3227*

The results of the modeling are shown in Figures 13–16. The best-fitting model has an inclination of $i = 60^\circ$ (fully consistent with that of the isophotes) and its black hole mass is $M_{\rm BH} = 1.5 \times 10^7$ (Fig. 13). The corresponding stellar mass-to-light ratios are $\Upsilon_{\rm bul} = 27.5$ and $\Upsilon_{\rm nuc} = 2.5$, respectively. As Figure 13 shows, the difference between $i = 60^\circ$ and 75° is formally only at the 1 σ level. In any case, the best-fit black hole mass does not depend strongly on the assumed inclination.

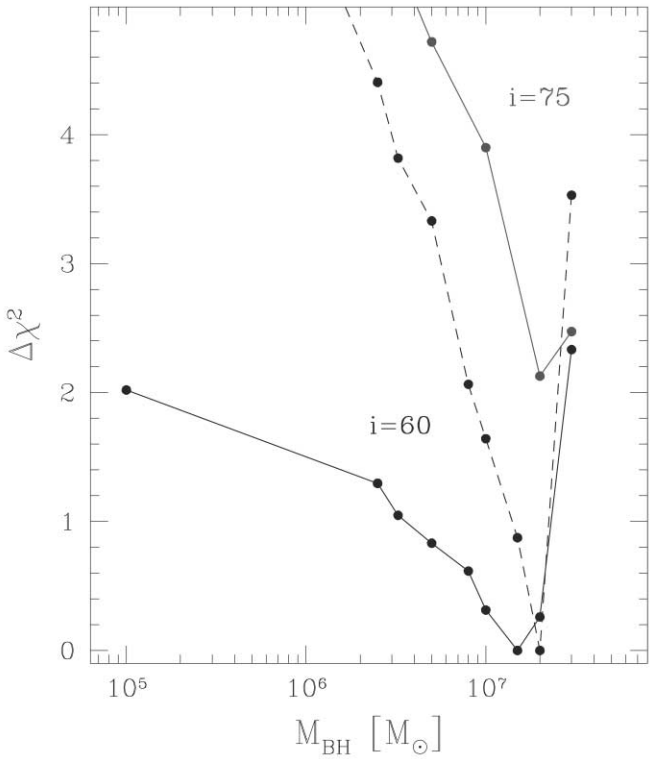

FIG. 13.—Goodness of fit $\Delta\chi^2 = \chi^2 - \min(\chi^2)$ vs. black hole mass (allowing the mass-to-light ratios of both the nuclear and bulge components to be optimized in the model each time, irrespective of external constraints): $i = 75^\circ$ and 60°. The dashed line shows the case for rescaled error bars in h_3 and h_4 (see text for details). [*See the electronic edition of the Journal for a color version of this figure*.]

It turned out after the modeling that the uncertainties assigned to h_3 and h_4 probably overestimate the actual freedom in the orbit distribution. From all calculated models we found the 68th percentiles $\chi^2_{h3}/N_{\rm data} = 0.01$ and $\chi^2_{h4}/N_{\rm data} = 0.06$, respectively. Consequently, the variations in the fitted models are much smaller than the originally allowed $\Delta h_3 = \Delta h_4 \equiv 0.1$. To illustrate the effect this has on the derived confidence intervals, we have rescaled these error bars to one-third of their original value and recalculated $\Delta\chi^2$. The result for the case $i = 60^\circ$ is shown by the dashed line in Figure 13. As apparent, it does not alter the best-fit black hole mass significantly but changes the confidence intervals drastically.

In the discussion above, we have allowed the Schwarzschild model to find the best mass-to-light ratios as free parameters. On the other hand, as previously intimated, these are in fact already limited by external constraints based on other arguments, leaving $M_{\rm BH}$ as the only truly free parameter. In particular, M/L_K for the bulge is unlikely to exceed 30 $M_\odot\ L_\odot^{-1}$ (Förster Schreiber et al. 2003), and the effective (stars plus gas) M/L_K for the nuclear component is likely to be in the range 1–5 $M_\odot\ L_\odot^{-1}$ (§ 6.3). It is for this reason that in Figure 14, which shows the dependencies between the three dynamical parameters, we have calculated confidence intervals for each pair of parameters assuming that the third is fixed. The combination of

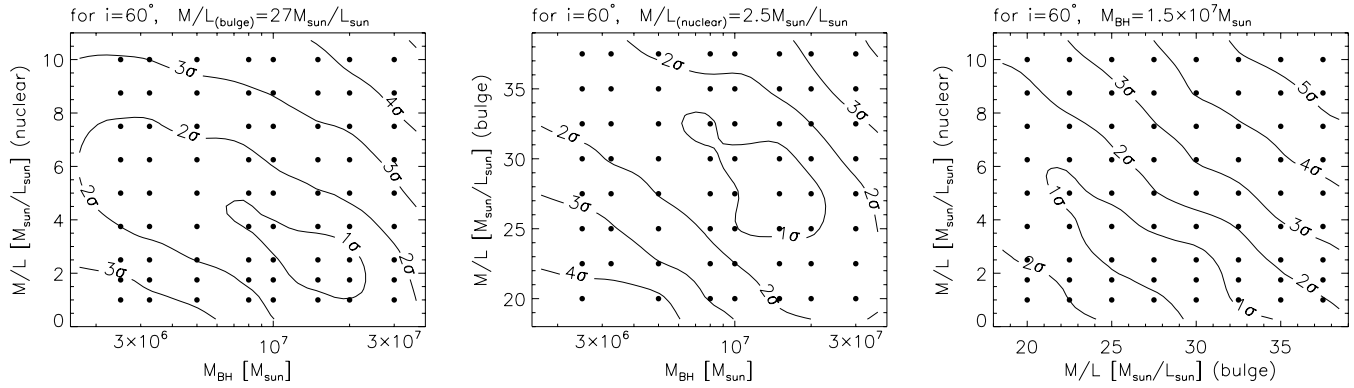

FIG. 14.—Range of models calculated (*black points*) and inferred confidence intervals (*contours*; in the range 1–5 σ corresponding to $\Delta\chi^2 = \{1, 4, 9, 16, 25\}$) for the Schwarzschild models calculated for the best-fitting inclination of 60°, with the third parameter in each case fixed at its optimal value. *Left*: As a function of $M_{\rm BH}$ and mass-to-light ratio of the nuclear component; *middle*: as a function of $M_{\rm BH}$ and mass-to-light ratio of the bulge; *right*: as a function of mass-to-light ratios of the bulge and nuclear component.

the degeneracies and the external constraints puts stronger limits on the range of possible black hole masses than the Schwarzschild modeling alone.

The figure shows a degeneracy between $\Upsilon_{\rm nuc}$ and $M_{\rm BH}$. Black hole masses of $M_{\rm BH} = 7\times10^6$–$2\times10^7\ M_\odot$ can be fitted with $\Upsilon_{\rm nuc} = 1$–$5\ M_\odot\ L_\odot^{-1}$. The reason for the degeneracy is illustrated in Figure 15: the nuclear component dominates the stellar mass density in the center inside 0.″1 and a larger $\Upsilon_{\rm nuc}$ can therefore compensate a lower $M_{\rm BH}$. Since its contribution to the central mass density is lower, the bulge $\Upsilon_{\rm bul}$ is less dependent on the black hole mass. But due to their similar light profiles around 1.″0, the bulge and nuclear mass-to-light ratios are coupled strongly to each other. From Figure 14 we find that the M/L_K ratio for the bulge should lie in the range $\Upsilon_{\rm bul} = 25$–$35\ M_\odot\ L_\odot^{-1}$, and much higher ratios are unlikely. This is within the range mentioned above and gives us confidence that the model is converging on a physically meaningful solution.

In summary, we conclude that the range of $M_{\rm BH}$ we derive, which we stress again is rather large due to the uncertainties discussed in § 5.1.2, is reasonably robust to the uncertainties in the input parameters. The limits of the range are set not only by the Schwarzschild models themselves but also by additional constraints on the mass-to-light ratios that, through degeneracies between the parameters, affect the black hole mass. The upper end is consistent with, although still less than, the other mass estimates mentioned at the start of the section, while the lower end is an order of magnitude smaller, suggesting that these techniques may tend to overestimate the black hole mass. Nevertheless, the preferred black hole mass we derive via Schwarzschild modeling is within a factor of 2–3 of the masses found by other

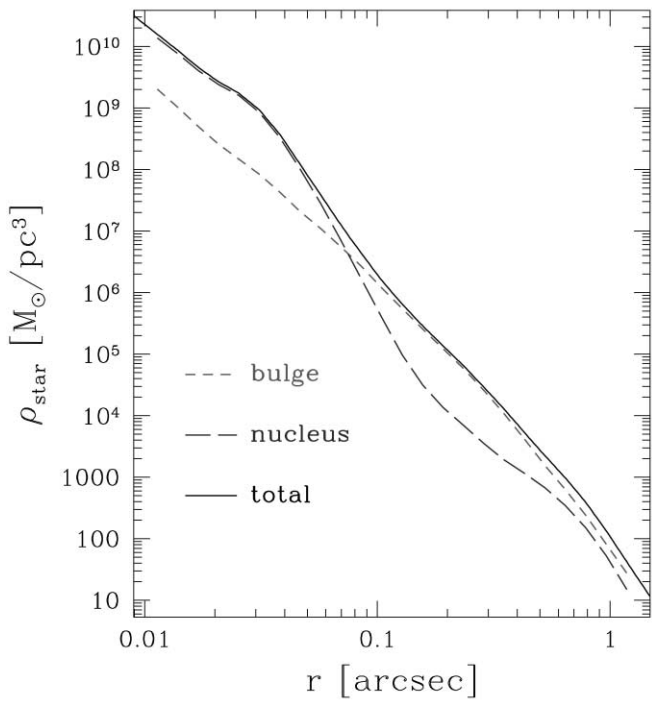

FIG. 15.—Best-fit stellar mass density and its decomposition into the bulge and nuclear component, respectively. [*See the electronic edition of the Journal for a color version of this figure.*]

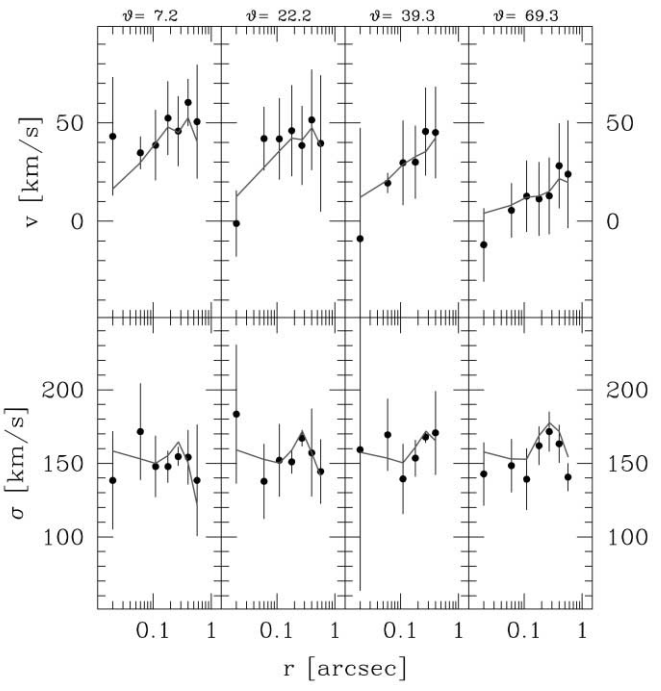

FIG. 16.—Comparison of model and data velocity (*top*) and dispersion (*bottom*). The four panels from left to right represent the 4 angular bins (from major axis at left to minor axis at right), the midpoints of which are indicated at the top. [*See the electronic edition of the Journal for a color version of this figure.*]

means and suggests that all methods are reasonable at least to this level of accuracy. With respect to the $M_{\rm BH}$-σ_* relation, it is interesting that, in contrast to NGC 3227, where we have found above that the stellar dynamical mass is a factor of a few less than the relation predicts, the equivalent mass for Cen A (Silge et al. 2005) is a factor of several greater. This suggests that, while the $M_{\rm BH}$-σ_* relation may be useful for order-of-magnitude $M_{\rm BH}$ estimates, the scatter for active galaxies may be significantly larger than that for quiescent galaxies.

6. MOLECULAR GAS AND THE TORUS IN NGC 3227

The 1–0 $S(1)$ morphology in Figure 3 is remarkably complex. As has been noted by Schinnerer et al. (2000) and Baker (2000) on larger scales for the cold molecular gas, we now find on smaller scales for the hot molecular gas that the nucleus itself is not identified with the strongest emission. The distribution is rather elongated at a position angle of -45° (we note that there are inherent uncertainties and difficulties due to the continuum subtraction associated with the 100° reported by Quillen et al. [1999] and the 45°–70° from Fernandez et al. [1999]). It is tempting to interpret the emission in terms of a bar and arclets. However, the kinematics and particularly the surprisingly high velocity dispersion of 100–125 km s^{-1} argue against it; a more natural interpretation is in terms of a highly turbulent medium, in which nevertheless the bulk of the gas follows uniform rotation. There do appear to be some nonrotational motions, but associated only with weaker 1–0 $S(1)$ emission and restricted to the galaxy's minor axis. This may indicate that some of the hot H_2 is influenced by outflows, or that the emission from hot gas that we see here does not reflect well the distribution of the cold gas. Figure 4 shows that the velocity field of the brighter emission, corresponding to $\frac{2}{3}$ of the flux in our field of view and hence also the bulk of the gas mass, exhibits pure rotation. These facts lead one toward the conclusion that most of the gas in the nucleus probably exists in a thick rotating disk.

Figure 17 supports this interpretation. It shows the rotation velocity $V_{\rm rot}$, corrected for inclination, and the dispersion σ for the molecular gas. The CO (2–1) data (Schinnerer et al. 2000) at larger scales and the SINFONI data on smaller scales are fully consistent. Also shown is the local $V_{\rm rot}/\sigma$ ratio (rather than the global version, which compares the maximum rotation velocity to the central dispersion). At $r \gtrsim 1''$ the ratio $V_{\rm rot}/\sigma$ clearly implies that the gas lies in a thin disk. At smaller radii, the ratio decreases smoothly, indicating that the gas distribution becomes geometrically thicker with respect to the radial scales.

6.1. *Star Formation, Molecular Gas, and the Torus*

Above we argue that the gas lies in a thick disk, and in § 4.2 that this is also the most likely distribution for the stars. Although the morphologies appear different (the stellar continuum is more centrally concentrated and the isophotal P.A. is closer to north), much of this arises from the bulge contribution to the light. Crucially, the kinematics for the gas and stars is remarkably similar: the clear velocity gradient at a P.A. of -30° to -45°, and the high dispersion of more than 100 km s^{-1}. The similarity of the velocity fields is emphasized in Figure 18, which shows that the only significant difference between the stellar and gas velocities occurs out along the minor axis where outflows may perturb the gas. Because they exist on similar spatial scales of a few tens of parsecs and exhibit similar kinematics, we conclude that the stars and gas are physically mixed.

Scales of a few tens of parsecs are exactly those on which theoretical models predict the obscuring torus should lie (Pier & Krolik 1992b, 1993; Granato & Danese 1994; Nenkova et al. 2002; Schartmann et al. 2005). In addition, an important property of the torus is its ability to collimate the UV radiation from the AGN to produce ionization cones whose apex lies close to the AGN, i.e., it is geometrically thick. We have argued that our data show that the gas and stellar distributions are thick. Our further conclusion is therefore that the gas and stars we see in the nucleus of NGC 3227 represent much of what is understood by the term "obscuring torus."

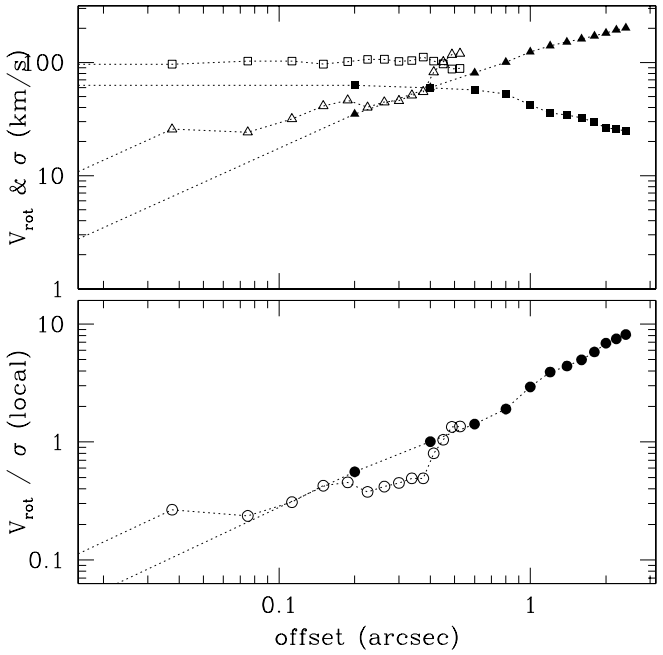

FIG. 17.—Gas kinematics from the CO (2–1) data of Schinnerer et al. (2000) and our SINFONI H_2 1–0 $S(1)$ data (*filled and open symbols, respectively*). Both are extracted along their kinematic major axis, with the two sides averaged. *Top*: Rotation velocity $V_{\rm rot}$ (*triangles*) and dispersion σ (*squares*). *Bottom*: Local $V_{\rm rot}/\sigma$ ratio increases smoothly with radius. The differences between the two data sets are primarily due to the beam sizes (0.″6 and 0.″085, respectively).

The idea of a star-forming torus is not new and has already been modeled by Wada & Norman (2002) and Wada (2005)[6] in response to the evidence that about half of Seyfert 2 nuclei have a nuclear starburst. However, from this work and that presented by Davies et al. (2004a, 2004b), it is now becoming clear also for type 1 Seyfert nuclei that star formation on scales associated with the torus is an energetically important process.

If the gas associated with the 1–0 $S(1)$ emission were indeed part of the obscuring torus, it would need to have a third crucial property: a high column density. We address this issue in § 6.3, but we first consider below how the vertical height of the gas distribution might be maintained.

6.2. *Supporting the Vertical Thickness of the Torus*

That the torus in NGC 3227 is vertically extended is clear from Figure 17: the ~100 km s^{-1} velocity dispersion of the gas is larger than its inclination-corrected rotational velocity out to radii of 30–40 pc. Even the lower CO (2–1) dispersion of ~60 km s^{-1} is still significant compared to the rotation velocity to these radii. Thus, the kinetic energy is dominated by random motions and implies a more spheroidal structure rather than

[6] See http://www.arcetri.astro.it/~agn2005/presentations/wada.pdf.

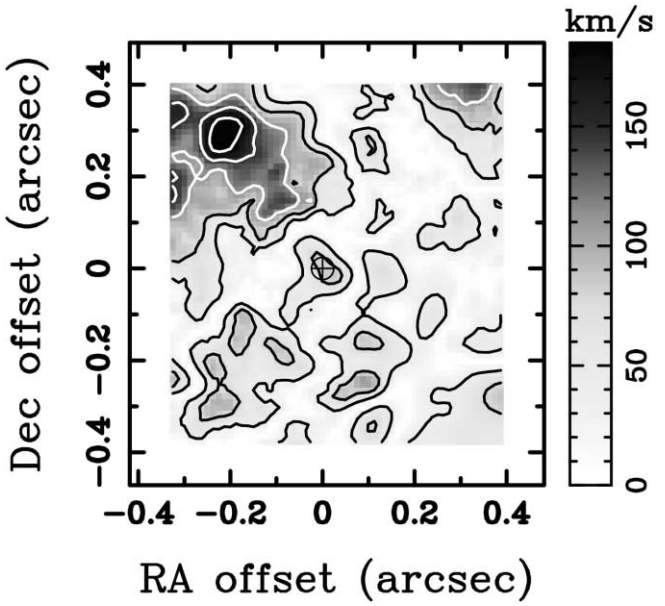

FIG. 18.—Absolute difference between the H_2 1–0 $S(1)$ and stellar velocity fields, with contours drawn at intervals of 25 km s^{-1}. The only major difference between the two is to the northeast, out along the minor axis. [*See the electronic edition of the Journal for a color version of this figure*.]

simple ordered rotation in a thin disk. Its constituent molecular clouds will undergo cooling via collisions on short timescales, comparable to the orbital period of a few million years. As a result, energy must be constantly injected into the interstellar medium (ISM) in order to maintain the vertical structure. The sources available to supply this energy are the AGN and the starburst, the latter via both radiation pressure and mechanically through supernovae. Such a situation may also provide, at least qualitatively, an answer to why the star formation should have stopped while there is still a large gas reservoir.

The effect of radiation pressure from the AGN itself has been explored by Pier & Krolik (1992a) and in their model depends primarily on the Eddington ratio of the black hole and the clumpiness of the torus. For the black hole mass, we adopt a value commensurate with our range found in § 5.1 and those from X-ray variability (Nikolajuk et al. 2004) and reverberation mapping (Onken et al. 2004), that is, $M_{\rm BH} = 2 \times 10^7\ M_\odot$. For the AGN luminosity, we take half of the bolometric luminosity since the other half is supplied by the nuclear starburst, that is, $L_{\rm BH} = 10^{10}\ L_\odot$. Since the Eddington luminosity $L_{\rm Edd} = 3.3 \times 10^4 M_{\rm BH}$ in solar units, this yields an Eddington ratio of $L_{\rm BH}/L_{\rm Edd} = 0.015$. This value is an order of magnitude smaller than the ratio of 0.1 that Pier & Krolik (1992a) found, which was needed for a smooth torus to be thick and static. On the other hand, for tori consisting of large clumps, they found that in the range $0.01 \lesssim L_{\rm Edd} \lesssim 0.1$ an equilibrium would exist for thick tori with $1 \gtrsim a/h \gtrsim 0.1$, where a is the inner radius and h is the full height in the body of the torus. In the case of NGC 3227 this could explain a thickness of up to a few parsecs but not the 10 to a few tens of parsecs implied by the velocity dispersion, unless the AGN was much more active in the recent past.

The possibility that supernovae might heat the molecular torus is treated specifically in the models of Wada & Norman (2002). However, because the coupling from supernova energy to kinetic energy of the ISM is rather weak, they used a very large supernova rate of $\nu_{\rm SN} \sim 1$ yr^{-1}. This is 2 orders of magnitude larger than the current rate in the central 60 pc of NGC 3227, which is already close to the maximum for our best-fitting star formation history. Hence, although they were able to reach scale heights for the torus of 10–20 pc, it seems unlikely that this could work for NGC 3227.

Recently, Thompson et al. (2005) have addressed the issue of whether radiation pressure from the starburst itself can provide the vertical support. For NGC 3227 it is not clear that their optically thick model can be applied, since we have argued in § 4.6 that the extinction must be low enough that even in the near-infrared the optical depth cannot exceed $\tau_{2.2} = 2.6$ and is probably no more than $\tau_{2.2} = 1$. In their optically thin limit, where the optical depth to UV photons is $\gtrsim$1 while to infrared photons from dust reprocessing it is $\lesssim$1, they derive the star formation rate necessary to maintain marginal Toomre stability ($Q \sim 1$), which for their model would give a scale height of $\sim$10 pc at a radius of 30 pc. If we assume a gas fraction of unity and $\sigma \sim 100$ km s^{-1} as measured for the 1–0 $S(1)$ line, we find that a star formation rate of $\sim 20\ M_\odot$ yr^{-1} would be needed. This is 2 orders of magnitude greater than the current rate derived in § 4.5 but only a factor of 6–7 more than the peak rate when the star formation was active. There are two ways to reconcile this difference. Using the 60 km s^{-1} dispersion of the CO (2–1) data of Schinnerer et al. (2000), one finds that the star formation rate necessary to maintain it is only 2.5 $M_\odot$ yr^{-1}. One could then argue that the higher dispersion of the 1–0 $S(1)$ line is due to the fact that this line traces only the hot gas and therefore will be strongly influenced by small-scale turbulence. Alternatively, one could argue that the gas fraction f_g is less than unity: for $f_g = 0.5$, one derives a star formation rate of 5 $M_\odot$ yr^{-1}.

Either of these alternative estimates is reasonably consistent with the peak rate derived from the observations. However, they are both still far greater than the current rate. It is perhaps conceivable that the molecular gas and star formation do not reach an equilibrium state. Instead, we speculate that what we are seeing is evidence for marginal Toomre stability: that once the gas cools, star formation may begin, but that once radiation pressure from the young stars is sufficiently high to heat the gas disk so that its turbulence increases and it thickens, star formation can no longer proceed. The molecular gas will then cool as the stars age and sink back into a thinner configuration, allowing the process to start again. To investigate this in a more quantitative sense, we have calculated the Toomre Q parameter, which is defined in the usual way as

$$Q = \frac{\sigma\kappa}{\pi G \Sigma},$$

where, using the data in Figure 17, σ is the velocity dispersion and κ is the epicyclic frequency. We have estimated the mass surface density Σ as follows. For the CO (2–1) data it is derived from the velocity curve under the approximation of Keplerian rotation in a thin disk. For our SINFONI 1–0 $S(1)$ data, we have considered two cases: Σ is constant within the area considered, and Σ follows the stellar light distribution, being centrally concentrated. For both of these we have assumed a total mass out to $r = 0\farcs5$ of $10^8\ M_\odot$ (see § 6.3). The true distribution will lie somewhere between these two extremes. The resulting estimates of Q are shown in Figure 19. The difference in Q derived from the 1–0 $S(1)$ and CO (2–1) data is a direct result of the differing σ apparent in Figure 17 and κ, which depends on the details of the rotation curve. What the figure shows is that as one approaches the nucleus from large radii of 1″–2″, Q increases, and within 0.″5 of the nucleus, on average $Q > 1$. Thus, the nuclear region does appear to be too dynamically hot to form stars. Based on

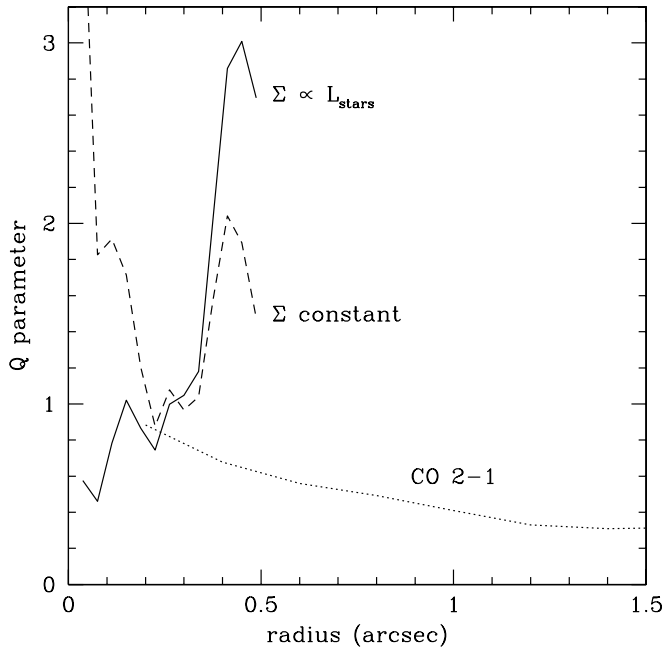

FIG. 19.—Calculation of the Toomre Q parameter, based on the kinematics in Fig. 17 for the CO (2–1) data and our SINFONI 1–0 $S(1)$ data. For the former, the mass surface density Σ is estimated under the assumption of Keplerian rotation in a thin disk; for the 1–0 $S(1)$ data we have considered the two extreme cases of Σ being either constant or following the centrally concentrated stellar distribution.

the star formation timescale we derived earlier, we suggest that the cycle of heating and cooling probably occurs on relatively short timescales of order 100 Myr. Thus, time-dependent modeling may be necessary if the geometry of the torus changes as the star formation or AGN fueling pass through successive active and quiescent phases.

6.3. *Mass and Column Density of the Gas*

The final thread in our analysis of whether the molecular gas in the nucleus of NGC 3227 can be identified with the obscuring torus concerns its column density. Our data trace only the hot $\gtrsim$1000 K H_2 through the 1–0 $S(1)$ line, for which our flux of 1.1×10^{-17} W m^{-2} in a 0.″8 aperture is consistent with that in Rodríguez-Ardila et al. (2004) and Quillen et al. (1999). Remarkably, it is possible to use this to make a reasonable estimate of the total molecular gas mass.

That there exists a relation between molecular mass and 1–0 $S(1)$ luminosity in actively star-forming galaxies should not be surprising, given that relations are already known between 1–0 $S(1)$ and infrared luminosity $L_{\rm IR}$ (Goldader et al. 1997) and between $L_{\rm IR}$ and CO luminosity $L_{\rm CO}$, which traces gas mass (Young & Scoville 1991). By comparing the 1–0 $S(1)$ line luminosities of 17 luminous and ultraluminous galaxies experiencing intense star formation (some of which also host an AGN) to gas masses derived from millimeter CO (1–0) luminosities, Mueller Sánchez et al. (2006) found that

$$M_{\rm gas}(M_\odot) \sim 4000 L_{1-0\,S(1)}(L_\odot) \quad \text{(mean)},$$

with a standard deviation of about a factor of 2. The exception to this was NGC 6240, which is known to be overluminous in 1–0 $S(1)$ and for which the scaling factor is by far the lowest, about an order of magnitude less than the typical value. The most likely reason for this is that the line does not originate in star formation but is due to cloud collisions resulting from the extreme turbulence in the gas (Sugai et al. 1997; Tacconi et al. 1999). This particular case therefore provides us with a way to estimate a conservative lower limit on the gas mass using

$$M_{\rm gas}(M_\odot) \sim 430 L_{1-0\,S(1)}(L_\odot) \quad \text{(NGC 6240)}.$$

For NGC 3227 this relation implies a gas mass in the central 0.″8 (65 pc) exceeding $4 \times 10^7\ M_\odot$ and perhaps as much as $(2\text{–}8) \times 10^8\ M_\odot$.

We now compare this range of estimates to three other constraints on the mass. In § 4.5 we found that the mass-to-light ratio of the stars in this same nuclear region is $M_*/L_K = 0.5\ M_\odot\ L_\odot^{-1}$, with a young stellar mass of $2.0 \times 10^7\ M_\odot$. On the other hand, the Schwarzschild modeling in § 5.1 implies that the most likely effective mass-to-light ratio including gas is $M_{\rm total}/L_K = 1\text{–}5\ M_\odot\ L_\odot^{-1}$. This result would imply a gas mass in the nuclear region of $M_{\rm gas} = (0.2\text{–}1.8) \times 10^8\ M_\odot$ and a most likely mass of about half this.

The mass estimated by Schinnerer et al. (2000) is rather less but did not include any correction to take into account the random motions inferred from the large velocity dispersion. We can make a rough estimate of the dynamical mass by including with the Keplerian $M = V_{\rm rot}^2 r/G$ the contribution of these random motions so that $M \propto V_{\rm rot}^2 + 3\sigma^2$ (where the factor 3 comes from a simple comparison of the kinetic energies associated with the two quantities). Taking from the CO (2–1) data in Figure 17 that $V_{\rm rot} = 50$ km s^{-1} at 0.″4 radius and $\sigma = 60$ km s^{-1}, we find $M \sim 1.2 \times 10^8\ M_\odot$.

Finally, in § 6.2 we argued that if radiation pressure does support the vertical thickness of the gas distribution, then the gas fraction may be only $f_g \sim 0.5$, implying equal masses of stars and gas. Thus, $M_{\rm gas}$ could perhaps be as low as $2.0 \times 10^7\ M_\odot$.

All of the estimates above point to the same range of masses, and so we can conservatively claim that the gas mass is most likely $(2\text{–}20) \times 10^7\ M_\odot$. While there is an order of magnitude uncertainty, this still has important implications. Assuming that the gas is uniformly distributed over the 0.″8 aperture, the mean column density through the entire region would be $n_{\rm H} = (0.8\text{–}8) \times 10^{24}$ cm^{-2}. If the gas does represent the torus, then such a large column should not be unexpected since there are many examples of type 2 AGNs for which hard X-ray observations indicate that the AGN itself is hidden behind similar amounts of gas, although it should be noted that the X-ray absorption may occur on very small scales. Two particularly well known cases are NGC 4945, for which the bright nuclear emission below $\sim$10 keV is completely blocked, implying an absorbing column of $\sim 5 \times 10^{24}$ cm^{-2} (Iwasawa et al. 1993; Done et al. 1996), and Circinus, for which the absorbing column was estimated to be $\sim 4 \times 10^{24}$ cm^{-2} based on the direct detection of X-rays at energies greater than 10 keV (Matt et al. 1999).

For a standard gas-to-dust ratio with $n_{\rm H}({\rm cm}^{-2}) = 1.5 \times 10^{21} \tau_V$, the column density implies an optical depth in the visual of $\tau_V > 500$. Since we are implicitly assuming that the stars are mixed with the gas rather than hidden behind a foreground screen, we must again use the mixed extinction model that we have used previously. Hence, we can compare directly the optical depth estimate here with the maximum possible to the stars of $\tau_V = 26$ from § 4.5. The two estimates are totally inconsistent with each other. The solution to this contradiction lies in the gas, instead of having a uniform distribution, being concentrated into clumps. If the clumps are sufficiently compact, then most lines of sight will not be intersected, and hence the stellar light

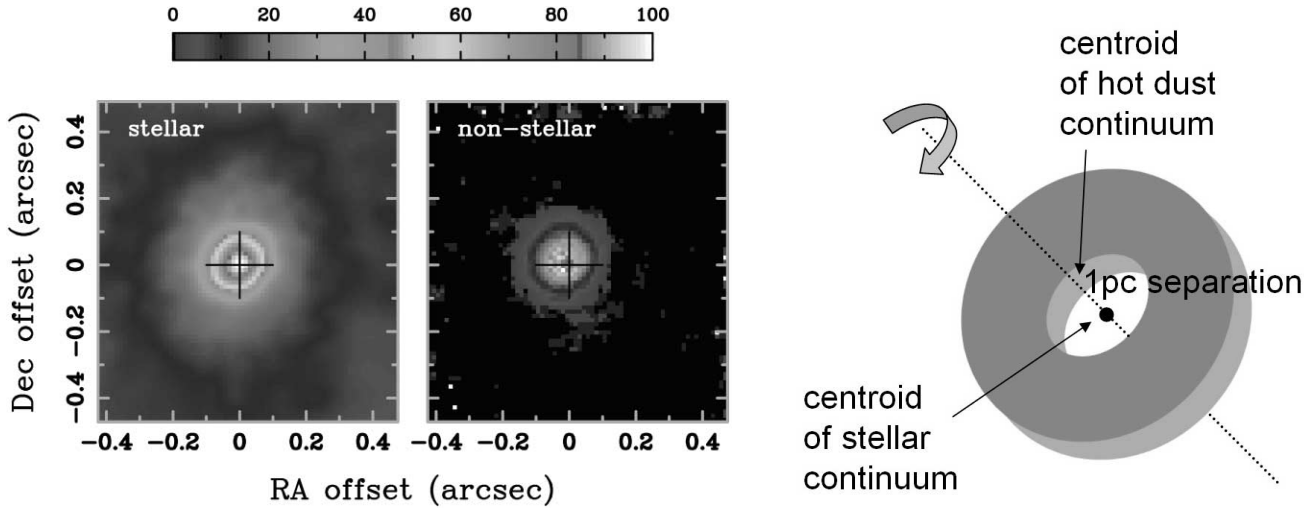

FIG. 20.—*Left and middle panels*: Images from the SINFONI data cube showing the stellar and nonstellar continua, both at 2.3 μm. The large cross on both panels indicates the center of the stellar continuum. The offset of the nonstellar continuum to the northeast is easily seen. *Right panel*: Cartoon of the canonical torus showing what might cause this offset. North is up and east is to the left. [*See the electronic edition of the Journal for a color version of the left and middle panels of this figure*.]

will suffer little extinction. The degree of clumpiness need not be extreme: even local increases in density of a factor of a few would be sufficient to reduce the covering factor of the gas to half, consistent with the maximum stellar extinction.

The gas density in these clumps will be high: the mean density over the whole region for a uniform distribution and assuming that the gas is extended vertically as much as it is laterally (i.e., by $\sim$60 pc) is $(4–40) \times 10^3$ cm^{-3}. This is already comparable to the typical densities in parsec-scale cores of molecular clouds. It is therefore no surprise that, as reported by Rodríguez-Ardila et al. (2004), the near-infrared H_2 line ratios indicate that the hot gas is thermalized.

In summary, we have used several independent mass estimates to put limits on the gas mass within 30 pc of the AGN. This mass implies very significant column densities of gas, easily sufficient to fulfill the third criterion of the obscuring torus mentioned in § 6.1. Thus, we can conclude that the gas we have observed via the 1–0 $S(1)$ is likely to be associated with the molecular torus. If so, then we have demonstrated that the gas in the torus is clumpy in nature and that the torus supports episodes of active star formation.

6.4. *The Inner Edge of the Torus*

A curious result from the data cube is that the 2.1 and 2.3 μm continuum centroids do not coincide. Since the stellar continuum increases to shorter wavelengths while the nonstellar continuum (i.e., hot dust emission associated with the AGN) increases to longer wavelengths, this can be most easily explained if these two continua are offset from one another. However, the scales involved are similar to those expected for differential refraction between the two wavelengths, about 0.″01, and this makes the two phenomena difficult to disentangle.

Instead, we can consider the separation of the continuum into its stellar and nonstellar components via the CO band heads longward of 2.3 μm. Because the two components are derived at the same wavelength, they are not susceptible to differential refraction. Yet the offset clearly remains, as shown in Figure 20: the nonstellar continuum is shifted by about 1 pixel (0.″0125 or 1 pc, approximately $\frac{1}{8}$ of the PSF size) to the northeast. This effect is not due to a few pixels that happen by chance to be brighter or fainter but is a systematic global shift of the entire feature and is significant with respect to the 0.05 pixel formal errors in each axis from a Gaussian fit to the respective profiles.

Our interpretation is that we are seeing directly the inner edge of the torus. We have shown this schematically with the cartoon in the right panel of Figure 20, where for simplicity we have drawn the torus as a uniform ring with sharp edges; this representation should not be taken too literally. If the torus is oriented in the same way as the larger (i.e., $\gtrsim$100 pc) scales, it will be inclined with its major axis on a line from southeast to northwest. As a result, the inner edge will only be visible on the far side; the near side will be hidden by the outer layers, since the torus is presumably optically thick. Regardless of whether the torus is modeled as a uniform or clumpy medium, its inner boundary is always expected to be a radius of $\sim$1 pc (e.g., Schartmann et al. 2005). This distance is set by the sublimation temperature of the dust grains, since they cannot exist any closer to the AGN. Depending on the thickness and inclination of the torus, one then would expect the centroid of the observable emission from the hottest dust grains (i.e., those at $\sim$1000 K, heated by the AGN rather than by stars) to lie at a projected distance of $\sim$1 pc from the AGN itself. In contrast, since star formation occurs throughout the torus, the centroid of the stellar continuum is centered on the AGN. Hence, one would expect to find, and indeed Figure 20 shows, an offset between the stellar and hot dust continua.

7. CONCLUSIONS

We have presented new near-infrared integral field spectroscopic data at 70 km s^{-1} FWHM spectral resolution of the Seyfert 1 nucleus in NGC 3227, making use of AO to reach a spatial resolution of 0.″085 (7 pc). In this paper we have addressed the issues of star formation and molecular gas around the AGN and their relation to the canonical obscuring torus, and we have analyzed the stellar kinematics using Schwarzschild models to determine the black hole mass. Our main conclusions are as follows:

1. The nuclear star-forming region around the Seyfert 1 nucleus is spatially resolved, on scales of a few parsecs to a few tens of parsecs. The most recent episode of intense star formation

began ~40 Myr ago but has now ceased. Within 30 pc of the AGN this starburst still accounts for 20%–60% of the galaxy's bolometric luminosity. Despite showing evidence for moderate rotation, the stars' kinetic energy is dominated by random motions indicating that they lie in a thick disk.

2. Schwarzschild modeling of the stellar kinematics leads to a black hole mass in the range $M_{\rm BH} = 7 \times 10^6 - 2 \times 10^7\ M_\odot$. The upper end is consistent with (although still less than) previous estimates made using other techniques. The large range arises through a degeneracy in whether mass is attributed to the black hole or the stars and gas, which can be resolved with better kinematic line profiles.

3. The gas in the central 80 pc of NGC 3227 exhibits several critical properties that are expected of a molecular obscuring torus: its spatial extent is a few tens of parsecs, it is geometrically thick, and it has column density of order $n_{\rm H} = 10^{24} - 10^{25}\ {\rm cm}^{-2}$. This argues that the gas we have observed is the torus. Moreover, based on the similarity of their spatial extents and their kinematics, it is likely that the gas and stars are physically mixed. Thus, the torus also supports episodes of active star formation.

4. It seems unlikely that the current level of AGN or star-forming activity can inject sufficient energy into the ISM to maintain the vertical thickness of the torus. However, this was possible when the star formation rate was at its peak value. We speculate that the torus may heat and subsequently cool, changing its vertical profile, as the star formation and AGN go through active and quiescent phases.

The authors are grateful to the staff at the Paranal Observatory for their support during the observations and to the entire SINFONI team at MPE and ESO. They are also indebted to Carole Mundell for kindly finding and rereducing the radio continuum data. Finally, we thank the referee for comments that helped improve the manuscript.

REFERENCES

Antonucci, R. 1993, ARA&A, 31, 473
Antonucci, R., & Miller, J. 1985, ApJ, 297, 621
Baker, A. J. 2000, Ph.D. thesis, Caltech
Begeman, K. 1989, A&A, 223, 47
Bonnet, H., et al. 2003, Proc. SPIE, 4839, 329
———. 2004, Messenger, 117, 17
Cameron, M., et al. 1993, ApJ, 419, 136
Cappellari, M., & Copin, Y. 2003, MNRAS, 342, 345
Chapman, S., Morris, S., & Walker, G. 2000, MNRAS, 319, 666
Cid Fernandes, R. 2004, in IAU Symp. 222, The Interplay among Black Holes, Stars, and ISM in Galactic Nuclei, ed. T. Storchi-Bergmann, L. Ho, & H. Schmitt (Cambridge: Cambridge Univ. Press), 127
Cid Fernandes, R., Heckman, T., Schmitt, H., González Delgado, R., & Storchi-Bergmann, T. 2001, ApJ, 558, 81
Condon, J. 1992, ARA&A, 30, 575
Davies, R., Sternberg, A., Lehnert, M., & Tacconi-Garman, L. 2003, ApJ, 597, 907
———. 2005, ApJ, 633, 105
Davies, R., Tacconi, L., & Genzel, R. 2004a, ApJ, 602, 148
———. 2004b, ApJ, 613, 781
Davies, R., Tacconi, L., Genzel, R., Ott, T., & Rabien, S. 2004c, Proc. SPIE, 5490, 473
Dehnen, W., & Gerhard, O. E. 1993, MNRAS, 261, 311
Done, C., Madjeski, G., & Smith, D. 1996, ApJ, 463, L63
Eisenhauer, F., et al. 2003a, Messenger, 113, 17
———. 2003b, Proc. SPIE, 4841, 1548
Fernandez, B., Holloway, A., Meaburn, J., Pedlar, A., & Mundell, C. 1999, MNRAS, 305, 319
Ferrarese, L., & Ford, H. 2005, Space Sci. Rev., 116, 523
Ferrarese, L., & Merritt, D. 2000, ApJ, 539, L9
Förster Schreiber, N. 2000, AJ, 120, 2089
Förster Schreiber, N., Genzel, R., Lutz, D., & Sternberg, A. 2003, ApJ, 599, 193
Garcia, A. 1993, A&AS, 100, 47
García-Burillo, S., et al. 2003, in ASP Conf. Ser. 290, Active Galactic Nuclei: From Central Engine to Host Galaxy, ed. S. Collin, F. Combes, & I. Shlosman (San Francisco: ASP), 423
Gebhardt, K., et al. 2000, ApJ, 539, L13
———. 2003, ApJ, 583, 92
Goldader, J., Joseph, R., Doyon, R., & Sanders, D. 1997, ApJ, 474, 104
González Delgado, R., Heckman, T., & Leitherer, C. 2001, ApJ, 546, 845
Goodman, J., & Tan, J. 2004, ApJ, 608, 108
Granato, G., & Danese, L. 1994, MNRAS, 268, 235
Greenhill, L., Gwinn, C., Antonucci, R., & Barvainis, R. 1996, ApJ, 472, L21
Greenhill, L., et al. 2003, ApJ, 590, 162
Gu, Q., Dultzin-Hacyan, D., & de Diego, J. 2001, Rev. Mex. AA, 37, 3
Heckman, T., González Delgado, R., Leitherer, C., Meurer, G., Krolik, J., Wilson, A., Koratkar, A., & Kinney, A. 1997, ApJ, 482, 114
Herrnstein, J., Greenhill, L., & Moran, J. 1996, ApJ, 468, L17
Horne, K., Peterson, B., Collier, S., & Netzer, H. 2004, PASP, 116, 465
Ivanov, V., Rieke, G., Groppi, C., Alonso-Herrero, A., Rieke, M., & Engelbracht, C. 2000, ApJ, 545, 190
Iwasawa, K., Koyama, K., Awaki, H., Kuneda, H., Makishima, K., Tsuru, T., Ohashi, T., & Nakai, N. 1993, ApJ, 409, 155
Jarrett, T., Chester, T., Cutri, R., Schneider, S., & Huchra, J. 2003, AJ, 125, 525
Johuet, B., Kunth, D., Melnick, J., Terlevich, R., & Terlevich, E. 2001, A&A, 380, 19
Kaspi, S., Maoz, D., Netzer, H., Peterson, B., Vestergaard, M., & Jannuzi, B. 2005, ApJ, 629, 61
Kaspi, S., Smith, P., Netzer, H., Maoz, D., Jannuzi, B., & Giveon, U. 2000, ApJ, 533, 631
Knapen, J. H. 2004, in Penetrating Bars through Masks of Cosmic Dust: The Hubble Tuning Fork Strikes a New Note, ed. D. Block et al. (Dordrecht: Kluwer), 189
Kormendy, J., & Kennicutt, R. C., Jr. 2004, ARA&A, 42, 603
Kormendy, J., & Richstone, D. 1995, ARA&A, 33, 581
Kronberg, P., Sramek, R., Birk, G., Dufton, Q., Clarke, T., & Allen, M. 2000, ApJ, 535, 706
Magorrian, J. 1999, MNRAS, 302, 530
Magorrian, J., et al. 1998, AJ, 115, 2285
Maraston, C. 2005, MNRAS, 362, 799
Marconi, A., & Hunt, L. 2003, ApJ, 589, L21
Martini, P., Regan, M., Mulchaey, J., & Pogge, R. 2003, ApJ, 589, 774
Matt, G., et al. 1999, A&A, 341, L39
Mazzarella, J., Voit, G., Soifer, B., Matthews, K., Graham, J., Armus, L., & Shupe, D. 1994, AJ, 107, 1274
Mueller Sánchez, F., Davies, R., Eisenhauer, F., Tacconi, L., Genzel, R., & Sternberg, A. 2006, A&A, in press
Mundell, C., Holloway, A., Redlar, A., Meaburn, J., Kukula, M., & Axon, D. 1995, MNRAS, 275, 67
Nelson, C., Green, R., Bower, G., Gebhardt, K., & Weistrop, D. 2004, ApJ, 615, 652
Nenkova, M., Ivezíc, Ž., & Elitzur, M. 2002, ApJ, 570, L9
Nikolajuk, M., Papadakis, I., & Czerny, B. 2004, MNRAS, 350, L26
Oliva, E., Origlia, L., Kotilainen, J., & Moorwood, A. 1995, A&A, 301, 55
Onken, C., Ferrarese, L., Merritt, D., Peterson, B., Pogge, R., Vestergaard, M., & Wandel, A. 2004, ApJ, 615, 645
Onken, C., Peterson, B., Dietrich, M., Robinson, A., & Salamanca, I. 2003, ApJ, 585, 121
Pedlar, A., Kukula, M., Longley, D., Muxlow, T., Axon, D., Baum, D., O'Dea, C., & Unger, S. 1993, MNRAS, 263, 471
Peterson, B., et al. 2004, ApJ, 613, 682
Pier, E., & Krolik, J. 1992a, ApJ, 399, L23
———. 1992b, ApJ, 401, 99
———. 1993, ApJ, 418, 673
Quillen, A., Alonso-Herrero, A., Rieke, M., Rieke, G., Ruiz, M., & Kulkarni, V. 1999, ApJ, 527, 696
Raha, N., Sellwood, J., James, R., & Kahn, F. 1991, Nature, 352, 411
Richstone, D., et al. 2004, ApJ, submitted (astro-ph/0403257)
Rigopoulou, D., Spoon, H., Genzel, R., Lutz, D., Moorwood, A., & Tran, Q. 1999, AJ, 118, 2625
Rodríguez-Ardila, A., Pastoriza, M., Viegas, S., Sigut, T., & Pradhan, A. 2004, A&A, 425, 457
Rodríguez-Ardila, A., & Viegas, S. 2003, MNRAS, 340, L33

Rovilos, E., Diamond, P., Lonsdale, C., Smith, H., & Lonsdale, C. 2005, MNRAS, 359, 827
Salamanca, I., et al. 1994, A&A, 282, 742
Schartmann, M., Meisenheimer, K., Camenzind, M., Wolf, S., & Henning, Th. 2005, A&A, 437, 861
Schinnerer, E., Eckart, A., & Tacconi, L. 2000, ApJ, 533, 826
———. 2001, ApJ, 549, 254
Schmitt, H., & Kinney, A. 1996, ApJ, 463, 498
Schwarzschild, M. 1979, ApJ, 232, 236
Shlosman, I. 2003, in ASP Conf. Ser. 290, Active Galactic Nuclei: From Central Engine to Host Galaxy, ed. S. Collin, F. Combes, & I. Shlosman (San Francisco: ASP), 427
Shlosman, I., & Begelman, M. 1989, ApJ, 341, 685
Silge, J., Gebhardt, K., Bergmann, M., & Richstone, D. 2005, AJ, 130, 406
Smith, H., Lonsdale, C., Lonsdale, C., & Diamond, P. 1998, ApJ, 493, L17
Sternberg, A. 1998, ApJ, 506, 721
Sternberg, A., Hoffmann, T., & Pauldrach, A. 2003, ApJ, 599, 1333
Storchi-Bergmann, T., González Delgado, R., Schmitt, H., Cid Fernandes, R., & Heckman, T. 2001, ApJ, 559, 147
Sugai, H., Malkan, M., Ward, M., Davies, R., & McLean, I. 1997, ApJ, 481, 186
Tacconi, L., Genzel, R., Tecza, M., Gallimore, J., Downes, D., & Scoville, N. 1999, ApJ, 524, 732
Thomas, J., Saglia, R., Bender, R., Thomas, D., Gebhardt, K., Magorrian, J., Corsini, E., & Wegner, G. 2005, MNRAS, 360, 1355
Thomas, J., et al. 2004, MNRAS, 353, 391
Thompson, T., Quartaert, E., & Murray, N. 2005, ApJ, 630, 167
Thornley, M., Förster Schreiber, N., Lutz, D., Genzel, R., Spoon, H., Kunze, D., & Sternberg, A. 2000, ApJ, 539, 641
Tremaine, S., et al. 2002, ApJ, 574, 740
Verma, A., Charmandaris, V., Klaas, U., Lutz, D., & Haas, M. 2005, Space Sci. Rev., 119, 355
Vestergaard, M. 2002, ApJ, 571, 733
———. 2004, ApJ, 601, 676
Wada, K. 2004, in Coevolution of Black Holes and Galaxies, ed. L. Ho (Cambridge: Cambridge Univ. Press), 186
———. 2005, in Superunification of AGN (Firenze: Astrophys. Obs. Arcetri)
Wada, K., & Norman, C. 2002, ApJ, 566, L21
Weiler, K., Panagia, N., Montes, M., & Sramek, R. 2002, ARA&A, 40, 387
Young, J., & Scoville, N. 1991, ARA&A, 29, 581